AIAA JOURNAL
Vol. 49, No. 9, September 2011

Development of Empirical Estimators for Feedback Control of High-Speed Axisymmetric Jets

Aniruddha Sinha,* Andrea Serrani,† and Mo Samimy‡
Ohio State University, Columbus, Ohio 43235

DOI: 10.2514/1.J050966

Localized arc filament plasma actuators have demonstrated significant potential in controlling high-speed and high-Reynolds-number axisymmetric jets in an open loop. As a first step in incorporating feedback for this control system, an empirical reduced-order model of the essential flow dynamics in the region surrounding the potential core of the unforced jet has been developed. An existing direct numerical simulation database, with a configuration similar to previous experiments, formed the testbed for this modeling phase. Real-time flow state estimation is a challenging problem in the implementation of feedback control for such complex flows of practical interest. Sensing the pressure in the irrotational near field close to the nozzle exit offers a suitable nonintrusive measurement that is driven by the jet's shear layer dynamics. Owing to convection, such a configuration naturally results in the measured pressure having a time lead compared with the state of the reduced-order model, which is very useful for feedback control. The sensing configuration used consists of an azimuthal ring array along with a linear array. Several estimation strategies are implemented and assessed using the numerical database. The time-invariant version of the linear Kalman filter is shown to have similar or better accuracy compared with a quadratic stochastic estimator, which in turn significantly outperforms a linear stochastic estimator. The filter is only as computationally complex as the linear stochastic estimator, thereby making it the strategy of choice.

Nomenclature

$E(\,)$	=	expectation operator
$\mathbf{F}$	=	linear state-transition matrix in discrete-time domain
k	=	index number in discrete time
m	=	azimuthal Fourier mode number
n	=	proper orthogonal decomposition mode index
N_c	=	number of discrete-time samples by which state estimate leads actual state
N_m	=	highest azimuthal Fourier mode retained
N_n	=	highest proper orthogonal decomposition mode retained
N_p	=	number of axially distributed pressure sensors in a particular type of array (ring or linear)
p	=	fluctuating pressure
r	=	radial coordinate
s	=	pressure array index
T_s	=	time interval between samples in discrete-time system implementation
x	=	axial coordinate with origin at nozzle exit
α	=	proper orthogonal decomposition modal coefficient
δ	=	Kronecker delta
ζ	=	normalized correlation coefficient
η	=	figure of merit for estimation fidelity of proper orthogonal decomposition modal coefficients
θ	=	azimuthal coordinate
Λ	=	proper orthogonal decomposition eigenvalue
$\boldsymbol{\Xi}$	=	covariance matrix of measurement model uncertainty
ξ	=	measurement model uncertainty
$\mathcal{X}_p$	=	set of axial coordinates of pressure sensors in particular type of array (ring or linear)
$\boldsymbol{\Psi}$	=	covariance matrix of dynamic model uncertainty
ψ	=	dynamic model uncertainty
$\underset{\sim}{(\,)}$	=	variant of azimuthal Fourier modal quantity that encompasses all modes
$\hat{(\,)}$	=	azimuthal Fourier transform
$\tilde{(\,)}_{k\backslash k'}$	=	estimated value at k given measurement at k'
$\tilde{(\,)}_{k/k'}$	=	estimated value at k given all measurements up to and including k'

Subscripts

EKF	=	quantity related to extended Kalman filter
KF	=	quantity related to Kalman filter
LSE	=	quantity related to linear stochastic estimation
LTIF	=	quantity related to linear time-invariant filter
QSE	=	quantity related to quadratic stochastic estimation

Superscripts

a	=	quantity related to pressure measured on azimuthal ring array of sensors
i	=	imaginary part of complex quantity
l	=	quantity related to pressure measured on linear array of sensors
r	=	real part of complex quantity
T	=	real transpose
$*$	=	complex-conjugate transpose

Received 29 September 2010; revision received 16 February 2011; accepted for publication 9 April 2011.

*Graduate Student, Department of Mechanical and Aerospace Engineering. Student Member AIAA.

†Associate Professor, Department of Electrical and Computer Engineering. Senior member AIAA.

‡Howard D. Winbigler Professor of Engineering, Department of Mechanical and Aerospace Engineering; samimy.1@osu.edu. Fellow AIAA (Corresponding Author).

I. Introduction

THE work presented here is an integral module of a larger effort devoted to controlling highly turbulent high-speed axisymmetric jets. The objective is mitigation of the noise propagating to the far field or enhancement of the bulk mixing to hasten dissipation. In either case, the large-scale structures in the shear layer of the jet must be manipulated [1,2]. Over the past several years, localized arc filament plasma actuators (LAFPAs) have been developed in the Gas Dynamics and Turbulence Laboratory (GDTL) at Ohio State University. These actuators have demonstrated considerable control authority on the said large-scale structures in open-loop control

experiments [3–5]. As in any control system, the performance of the LAFPAs in an open loop is a function of the jet operating conditions, which are subject to variations and uncertainties. Thus, a natural advancement toward practical implementation is to incorporate feedback control, which may guarantee robustness in the presence of such uncertainties.

A simple feedback control strategy is model-free extremum-seeking control. Several variants of this idea were developed and successfully implemented at GDTL [6]. However, since the dynamics of the system are ignored in a model-free controller, the responsiveness of the control system is limited. For improved responsiveness, a model-based controller is required that explicitly accounts for the dynamics. A necessary first step in this approach is to model the dynamics of the system without any actuation.

In [7], the authors proposed a strategy for educing such an unforced dynamical model from experimental data for the control system under consideration. In that work, a well-established direct numerical simulation (DNS) database [8] was employed for model development and validation. Two different models were created. The first model employed empirical data from the database directly, and it served as a benchmark. The second model employed a reduced database that was created by mimicking the practical constraints that would be posed by actual experiments. The simulated trajectories of both models were compared back to the original database, and the fidelity was deemed sufficient for the purposes of feedback control. In the present work, the first model would be employed; thus, it is will be briefly described along with some background information.

An incompressible flow is uniquely determined by specifying the three components of velocity over the entire flow domain. Considering compressibility effects, two additional thermodynamic variables (e.g., density and pressure) are needed for a full characterization of the flow. In control system terminology, this information constitutes the set of states of the system. Since the dynamics of these states are governed by the infinite-dimensional Navier–Stokes equations, infinitely many states are needed to fully specify the flow. Such a model is not useful for practical control implementation, and one pursues model-reduction strategies instead. In developing a reduced-order model (ROM), a change of coordinates is sought such that a small set of the new coordinates is required to approximately represent the original system. Proper orthogonal decomposition (POD) is the method of choice for reducing the order of flow kinematics using empirical data [9–11]. With this technique, the flow variables are projected onto the subspace spanned by the orthonormal spatial POD basis, and the new set of coordinates are the projection coefficients, also known as POD modal coefficients. Subsequently, one typically employs Galerkin projection (GP) to obtain the dynamics of the flow in these new coordinates [11]. This route was adopted in [7] to develop the dynamical model under discussion.

The ultimate goal of the present work is to incorporate feedback control for the plasma-actuated high-Reynolds-number jet. This jet has not been fully replicated in numerical simulations, although significant advances have been reported [12]. As such, the final empirical database for its reduced-order modeling must be experimental data, although the modeling strategy is being evaluated here using a numerical simulation database of appreciable fidelity. The database required for incorporating compressibility effects in the model has to be built by simultaneously acquiring the velocity and two other thermodynamic quantities over a domain of feasible size. To date, experimentalists have not realized this goal. These practical constraints impose the incompressibility assumption on the present ROM. The inaccuracies incurred by ignoring compressibility effects for the ROM under consideration have been shown to be within acceptable bounds [7].

Feedback control of a system requires real-time observation of the state of the system, which is rarely feasible. Instead, one typically must resort to estimating the state from a related output variable that can be measured. To control an incompressible jet, its instantaneous velocity field must be available to the controller. Real-time measurement of the velocity in a high-speed jet is not feasible. However, this velocity field is strongly correlated with the pressure in the irrotational near field of the jet [2,13–18]. The latter can be acquired in real time relatively nonintrusively and, being a scalar variable, it is easier to measure [17]. Thus, a more practical feedback control system would measure the pressure in the irrotational near field in real time and use it to estimate the velocity.

State estimation for closed-loop control is essentially a filtering operation. As such, it may be divided into the following categories:

1) The zero-memory, or single-time, variant involves using the measured output at each instant to directly estimate the state at that particular instant. This is the original form of stochastic estimation (SE), in which the state-output relation is determined by curve fitting.

2) The limited-memory estimation employs a finite backward-extended time history of outputs to approximate the state at any instant. This is the finite impulse response filter, or the multitime SE.

3) In the infinite-memory variant, the entire history of outputs measured up to a point in time is used for the recursive estimation of the state at that time; this is the infinite-impulse response (IIR) filter. The linear time-invariant filter (LTIF) and Kalman filter (KF) are popular members of this category.

SE was originally introduced to educe coherent structures in turbulent flows [19]. Subsequently, this technique has also been employed for estimating flow variables using minimal measurements and a knowledge of the spatial correlations in the flow. The earliest implementations were of linear SE (LSE) in the areas of isotropic turbulence [20], boundary layer [21], and axisymmetric jet shear layer [22]. In these works, the instantaneous velocity at various locations in the flow were approximated as separate linear functions of the velocities measured at the same instant at only a few locations. In a parallel development, higher-order SE (HOSE), including quadratic SE (QSE), were implemented for isotropic turbulence [23,24] and the boundary layer [21]. These studies generally concluded that, compared with LSE, the marginal improvements in accuracy of estimation with HOSE did not warrant the added complications of computing the higher-order statistical moments.

Numerous researchers have advanced the original technique of SE in several significant directions. Instead of using measurements of the spatially sparse velocity field itself to estimate a spatially denser velocity field, measurements of other relevant flow quantities, viz., pressure and wall shear stress, have been used [14,25–32]. This modification typically reduces the complexity of experiments, since time-resolved velocity measurements are difficult and intrusive. As the solution of Poisson's equation indicates, the pressure field is related to the global velocity field. This implies that pressure–velocity correlations are strong across greater distances compared with velocity–velocity correlations. In the investigations where surface pressure was used in the estimation, significant improvements in accuracy were observed with QSE compared with LSE [25,26,30,31]. For the application to the turbulent boundary layer, this outcome was shown to indicate the comparable relevance of the mean-turbulent and turbulent–turbulent pressure source terms [25]. In the cavity flow configuration, it was posited that the higher-order terms were necessary, since the linear model becomes less accurate when the measurement location is far away from the estimation location [26].

Another development of SE is its coupling with POD to obtain a low-dimensional estimate of the flow kinematics. In the classical version of the complementary technique, the velocity field obtained through LSE was further filtered using POD [33,34]. In the modified complementary SE, the POD modal coefficients of the velocity field were first estimated using a different flow variable (say, the pressure or wall shear stress) followed by a POD reconstruction of the velocity field from these estimates [14,17,27,28,30,31,35]. The concept was later extended by decomposing both the measured field and the field to be estimated into their respective low-dimensional spatial modes (be they Fourier and/or POD) before linking the corresponding modal coefficients through SE [17,36]. The successive modifications were implemented to take advantage of the implicit spatial filtering and the increased correlations between the low-dimensional quantities while reducing computations.

The preceding discussion focused on the single-time version of SE. In single-time-delay SE, a delayed version of the measurement is

used to estimate the field at any given time [21,25]. This is useful where the timescales of the measurement and estimate are alike, but a fixed predetermined convective delay has to be considered. On the other hand, multitime SE uses measurements over a finite moving window stretching back in time for estimating the present state [30,37]. This accounts for convection effects in the flow while also taking advantage of the temporal persistence of the large-scale structures being estimated. Although the accuracy of estimation first improves with the size of the time window, the fidelity actually degrades quite rapidly beyond a certain size [37]. Thinking from the perspective of polynomial curve fitting, this may be explained by the overdetermination of the fit of a high-degree polynomial in the absence of enough independent realizations. In real-time estimation, the number of delays in discrete time that can be considered is typically limited by hardware constraints.

Extending the concept of multitime SE to the limit of theoretically infinite time, one arrives at the spectral variant of SE. This technique may be implemented for statistically stationary flows where the correlation is computed in the temporal Fourier domain [17,29,34,36]. The spectral SE is especially useful whenever the spectral features of the measured and estimated variables are disparate and/or significant time delays exist between them [29]. In practical implementations, one is typically limited to a finite time window, but this has to be long enough for satisfactory resolution of the frequency content. Moreover, its nonrecursive nature and the necessity of computing the temporal Fourier transform restrict the spectral SE to offline estimation applications.

The preceding discussion highlights the need for a recursive filtering technique that would address the dynamics of the flow while avoiding the hardware constraints of limited memory. This is the essence of an IIR filter like the KF [38–40]. However, unlike SE, IIR filters need a model of the flow dynamics. Such a model is precisely the ROM discussed. One of the advantages of a model-based filter over a stochastic estimator is the inherent noise-filtering properties of the former [41]. In essence, by incorporating some predictive knowledge of the system, model-based filters may separate the noise from the signal. On the other hand, stochastic estimators typically pass through the unfiltered measurement noise to the state estimate. A different model-based technique is adjoint-based model predictive estimation [41]. Typically, this strategy is quite computation intensive, and hence may not be as suitable for real-time control implementation as an IIR filter.

Owing to the need for a ROM of the flow dynamics, implementing a model-based state estimation is a challenge. Estimation of narrowband frequency fluid dynamics has been reported by several investigators [42–44]. These typically focus on a few states, and the benefits of dynamic estimation over SE are easily demonstrated. In two recent contributions to the field of broadband fluid dynamic estimation, the use of KFs has been proposed to estimate the full state of a channel flow, given spatially resolved measurements of the two-component wall shear stress and wall pressure everywhere on the surfaces [45,46]. Previously, it had been shown that a theoretically complete information of the flow can be deduced from this set of measurements [41]. Such comprehensive measurements are rarely feasible in unbounded flows, and one has to settle for far greater approximations. The present work proposes effective strategies in such a challenging situation.

The first implementation of LSE for the axisymmetric jet employed a linear array of near-field microphones to estimate the axial and radial velocities in the shear layer that were a priori measured using hot wires [14]. In a subsequent effort, a similar microphone setup was used, but the velocity was measured using two-component particle image velocimetry (PIV) in a meridional plane [32]. This work demonstrated that QSE substantially improves the estimation of the turbulent kinetic energy. The next development in this area was to employ an azimuthal ring array of sensors in the near field simultaneously with laser Doppler anemometry in the shear layer [29]. This research also introduced the technique of spectral LSE (SLSE). In a recent contribution, the pressure was measured on a similar azimuthal ring array and the velocity was measured on multiple cross-stream slices with stereo-PIV [17]. In this effort, both the pressure and velocity fields were reduced to their low-dimensional azimuthal Fourier modes and the velocity was additionally represented using POD, before SLSE was applied. The present work builds on these techniques but with a focus on real-time state estimation. The two main contributions of this paper are the development of a KF for infinite-memory estimation and the formulation of QSE in the Fourier azimuthal domain, both in the context of an axisymmetric jet shear layer.

A very useful (and, in fact, indispensable) tool for evaluating the various estimation strategies is a time-resolved and spatially resolved three-dimensional volumetric database of the axisymmetric jet. Freund [8] has performed a DNS of an unforced Mach 0.9 axisymmetric jet with Reynolds number based on a jet diameter (Re) of 3600. In spite of its low Reynolds number, most of its general characteristics, and especially the nature of its large-scale structures, were found to be similar to those of a Mach 1.3 jet with an Re of 1.1×10^6 in an experiment [47]. This database was used to develop and validate the reduced-order modeling strategy in [7]. In the present paper, the DNS database is used to assess various strategies for estimating the state of the ROM.

A brief review of the ROM of the jet appears in Sec. II. The various strategies for real-time state estimation are laid out in Sec. III. These strategies are assessed in simulation, and the results are presented in Sec. IV. Concluding remarks are offered in Sec. V.

II. Modeling of Jet Dynamics

The flow domain of the axisymmetric jet is unbounded; the first step in model order reduction is to choose a bounded region that is most pertinent for the control objectives at hand. An appropriate choice is a cylindrical domain covering the shear layer in the vicinity of the end of the potential core, as shown in Fig. 1. A reduced-order dynamic model of the flow in this region was developed in [7]; the procedure will be briefly reviewed here. Before introducing the notation for this model, the relevant normalizations are established.

Let the jet exit velocity and nozzle exit diameter be U_{jet} and D, respectively. All velocities and linear coordinates are implicitly normalized by these respective quantities. Time is normalized by the flow timescale D/U_{jet}. Pressure is normalized by $\rho_{\text{jet}} U_{\text{jet}}^2$, where ρ_{jet} is the jet exit density. With the kinematic viscosity of the jet at exit denoted by ν_{jet}, the pertinent Reynolds number is $Re := U_{\text{jet}} D/\nu_{\text{jet}}$.

Employing cylindrical coordinates $\mathbf{x} := (x, r, \theta)^T$, the modeling domain is $\Omega := [X_1, X_2] \times [0, R] \times \mathbb{T}$. Here, X_1 and X_2 denote the

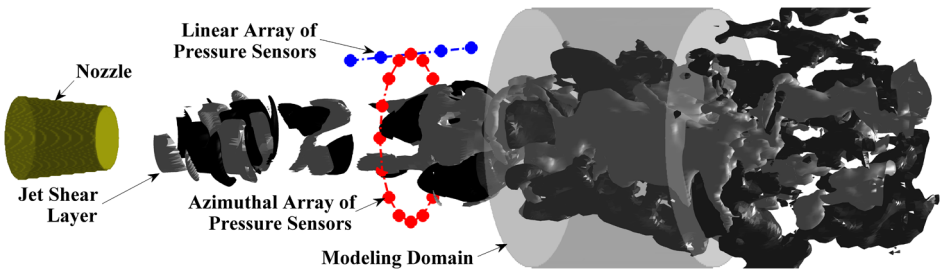

Fig. 1 Schematic of axisymmetric jet indicating modeling domain and model-state estimation strategy.

upstream and downstream bounds of the axial domain, R is the radial extent of the domain, and $\mathbb{T}$ is the circle group. The velocity vector is $\mathbf{U}$: $\Omega \times \mathbb{R} \to \mathbb{R}^3$ and $\mathbf{U}$: $(\mathbf{x}, t) \mapsto (U_x, U_r, U_\theta)^T$. The statistical stationarity and axisymmetry of the jet are used to define the mean velocity field as

$$\bar{\mathbf{U}}(x, r) := E\left\{\frac{1}{2\pi}\int_{-\pi}^{\pi} \mathbf{U}(x, r, \theta, t)\, \mathrm{d}\theta\right\}$$

Henceforth, unless otherwise mentioned, the expectation operator $E(\cdot)$ will signify the ensemble average. From the symmetry $\bar{U}_\theta \approx 0$, and this is enforced explicitly in the implementation. The fluctuating velocity vector is defined as $\mathbf{u}(x, r, \theta, t) := \mathbf{U}(x, r, \theta, t) - \bar{\mathbf{U}}(x, r)$, with the three components being u_x, u_r, and u_θ, respectively.

The azimuthal direction is homogenous and periodic, so that any generic flow variable $w(\theta)$ lends itself to the azimuthal Fourier transform pair denoted by $w(\theta) \overset{\mathcal{F}_m}{\mapsto} \hat{w}(m)$:

$$\hat{w}(m) := \frac{1}{2\pi}\int_{-\pi}^{\pi} w(\theta) e^{-im\theta}\, \mathrm{d}\theta$$

Here, m is the azimuthal mode. The inverse Fourier transform will be denoted by $\hat{w}(m) \overset{\mathcal{F}_\theta}{\mapsto} w(\theta)$:

$$w(\theta) = \sum_{m=-\infty}^{\infty} \hat{w}(m) e^{im\theta}$$

With this, $\mathbf{u}$ is transformed as $\mathbf{u}(x, r, \theta, t) \overset{\mathcal{F}_m}{\mapsto} \hat{\mathbf{u}}(x, r, t; m)$. The highest azimuthal mode that can be resolved is limited by the azimuthal grid resolution. Moreover, typically, the higher azimuthal modes are dynamically insignificant. So, in the remainder of the paper, the azimuthal modes would be taken in the truncated range $m \in [-N_m, N_m]$.

The fluctuating velocity field $\mathbf{u}(\cdot, t)$ belongs to the Hilbert space of square-integrable functions $\mathcal{L}^2_\Omega$ equipped with an inner product denoted by $\langle \cdot, \cdot \rangle_\Omega$. The goal of POD is, given an ensemble of data for $\mathbf{u} \in \mathcal{L}^2_\Omega$, to find a subspace $S \subset \mathcal{L}^2_\Omega$ of fixed dimension N_n, such that the error $E\{\|\mathbf{u} - \mathcal{P}_S \mathbf{u}\|^2\}$ is minimized [48]. Here, $\|\cdot\|$ is the induced norm on $\mathcal{L}^2_\Omega$, and $\mathcal{P}_S$ is the orthogonal projection onto the subspace S. The details of POD have been well-established elsewhere [9–11,48,49]. For the purpose of the present discussion, it is sufficient to state that, in the presence of the homogenous azimuthal direction, the POD devolves into the following integral eigenvalue problem for each azimuthal mode m [7]:

$$\int_{X_1}^{X_2}\int_0^R E\{\hat{\mathbf{u}}(x, r, t; m)\hat{\mathbf{u}}^*(x', r', t; m)\}\hat{\mathbf{\Phi}}^{(n)}(x', r'; m) r'\, \mathrm{d}r'\, \mathrm{d}x' = \Lambda^{(n)}(m)\hat{\mathbf{\Phi}}^{(n)}(x, r; m) \tag{1}$$

The quantities Λ and $\hat{\mathbf{\Phi}}$ are, respectively, the eigenvalue and eigenfunction for the nth POD mode. The asterisk denotes the adjoint operation, which reduces to the complex-conjugate transpose for our purpose.

The POD mode number indexes the real nonnegative eigenvalues in descending order. Then, the first N_n eigenfunctions form the desired optimal basis for the subspace S. This allows the following approximate change of coordinates for each azimuthal mode m:

$$\hat{\mathbf{u}}(x, r, t; m) \approx \sum_{n=1}^{N_n} \alpha^{(n)}(t; m)\hat{\mathbf{\Phi}}^{(n)}(x, r; m) \tag{2}$$

where the nth POD modal coefficient is computed as

$$\alpha^{(n)}(t; m) = \int_{X_1}^{X_2}\int_0^R \hat{\mathbf{\Phi}}^{(n)*}(x, r; m)\hat{\mathbf{u}}(x, r, t; m) r\, \mathrm{d}r\, \mathrm{d}x \tag{3}$$

The POD modal coefficients have the well-known property [11,48]

$$E\{\alpha^{(n)}(t; m)\alpha^{(n')*}(t; m')\} = \Lambda^{(n)}(m)\delta_{m,m'}\delta_{n,n'} \tag{4}$$

where δ is the Kronecker delta.

Remark 1: Using the preceding property along with the properties of the Fourier transform, one may derive the following:

$$E\{\alpha^{(n),r}(t; m)\alpha^{(n),r}(t; m)\} = E\{\alpha^{(n),i}(t; m)\alpha^{(n),i}(t; m)\} = \frac{\Lambda^{(n)}(m)}{2} \quad \forall\ m \neq 0 \tag{5a}$$

$$E\{\alpha^{(n),r}(t; m)\alpha^{(n),i}(t; m)\} = 0 \tag{5b}$$

$$\alpha^{(n)}(t; -m) = \alpha^{(n)*}(t; m) \tag{5c}$$

In the preceding equations, the superscripts r and i, respectively, denote the real and imaginary components of the complex modal coefficient.

The preceding discussion focused on the reduced-order modeling of the flow kinematics; the dynamics will be considered next. The incompressible Navier–Stokes equations governing the flow can be formally written as $\dot{\mathbf{U}} = \mathcal{N}(\mathbf{U})$, where $\mathcal{N}$ is a vector field on $\mathcal{L}^2_\Omega$. The goal of reduced-order dynamics modeling is, given the finite-dimensional subspace S of $\mathcal{L}^2_\Omega$, to determine a dynamical system that evolves on S and approximates the original dynamics in some sense [48]. GP specifies the new vector field on S as the orthogonal projection of $\mathcal{N}$ onto S.

It was shown in [7] that the application of GP to the axisymmetric jet results in the following set of coupled quadratic ordinary differential equations (ODEs) that govern the evolution of the POD modal coefficients

$$\dot{\alpha}^{(n)}(t; m) = \sum_{n'=1}^{N_n} f_{nn'}(m)\alpha^{(n')}(t; m) + \sum_{m'=m-N_m}^{N_m}\sum_{n',n''=1}^{N_n} \alpha^{(n')}(t; m') \times g_{nn'n''}(m', m - m')\alpha^{(n'')}(t; m - m') \tag{6}$$

The time-independent coefficients f and g were determined from the POD eigenfunctions and the mean velocity profile $\bar{\mathbf{U}}$, both of which were extracted from the empirical database. It is important to note that, although the POD modal coefficients are in the complex domain, f and g are real [7]. For model-based feedback control of the jet, Eq. (6) represents the requisite ROM of the dynamics in state-space form. It is clear that the POD modal coefficients constitute the state to be estimated in real time.

The preceding ROM was developed as a first step toward feedback control of a complicated flow; hence, it does not incorporate actuation effects. Actuation effects typically enter into such a ROM in two ways: as an explicit additive term and through a possible choice of a different POD basis that better represents the actuated flow state [30,50–52]. Neither of these modifications detract from the usefulness of the unactuated model for the estimation strategy development pursued herein. Since the additive actuation term is known at all times, it can be incorporated in the estimation model directly. Moreover, although the choice of a different basis would change the coefficients of the unactuated ROM, the estimation strategy itself would not be affected.

Since the feedback control will be implemented in discrete time, the continuous dynamics must be converted to a sampled dynamical system. The appropriate sampling rate for the present implementation is the rate at which data were saved in the DNS database; this would be denoted by T_s. The sampled version of the state of the ROM is denoted by $\alpha^{(n)}_k(m) \equiv \alpha^{(n)}(t = kT_s; m)$, where $k \in \mathbb{N}$ is the set of natural numbers. For each individual azimuthal mode, the state vector is defined as

$$\boldsymbol{\alpha}_k(m) := [\,\alpha^{(1)}_k(m) \quad \cdots \quad \alpha^{(N_n)}_k(m)\,]^T \tag{7}$$

III. Estimator Modeling

For a practical implementation of real-time estimation for a jet, the pressure sensors must be located near the nozzle exit. However, the velocity field is to be estimated in a domain that is further downstream in the vicinity of the end of the potential core (see Fig. 1). Owing to convection, the estimate from such a configuration would lead the actual velocity field in time. This is very useful for feedback control. The ensuing formulation considers a unique value of the time lead represented by $N_c T_s$. A method is proposed for determining the actual value of N_c in Sec. IV.

Two main approaches are taken for real-time estimation of the state of the jet shear layer in Eq. (6). In the first approach, single-time-delay modified complementary SE is used to directly estimate the POD modal coefficients as a function of the pressure measured in the irrotational near field, with the time separation being $N_c T_s$. Both linear estimation and QSE are evaluated. This procedure does not use the known dynamics of the jet as captured by the model of Eq. (6). Alternatively, a KF is implemented that uses the derived ROM of the jet, as well as a static output equation that expresses the near-field pressure at any instant of time t as a linear function of the POD modal coefficients at time $t + N_c T_s$. It is not trivial to obtain the said output equation from first principles. One option is to extend the incompressibility assumption made in the derivation of the ROM to argue for the approximate validity of Poisson's equation for pressure, which may then be explicitly solved in real time [53]. A novel contribution of the present work is to employ SE to derive this equation from empirical data. Note that this represents the inverse of the SE problem for state estimation.

With reference to Fig. 1, consider N_p^a azimuthal arrays of pressure transducers arranged at different axial locations $x \in \mathcal{X}_p^a$. In addition, suppose that there are N_p^l individual pressure sensors at different axial locations $x \in \mathcal{X}_p^l$ that do not belong to any azimuthal array. Although the development does not need the individual sensors to form a linear array, they would be assumed to be in a straight line at $\theta = 0$ for notational convenience. Without loss of generality, it is also assumed that all pressure sensors are located on the surface of a virtual cone coaxial with the jet, so that their radial locations are a function of their axial locations.

The individual pressure signals from the sensors in the azimuthal arrays are denoted as $P^a\colon \mathbb{T} \times \mathbb{R} \times \mathcal{X}_p^a \to \mathbb{R}$ and $P^a\colon (\theta, t; x) \mapsto \mathbb{R}$. In discrete time, the notation is $P_k^a(\theta; x) \equiv P^a(\theta, t = kT_s; x)$, where $k \in \mathbb{N}$. As before, the mean and fluctuating pressure are defined as

$$\bar{P}^a(x) := E\left\{\frac{1}{2\pi}\int_{-\pi}^{\pi} P_k^a(\theta; x)\, \mathrm{d}\theta\right\}$$

and $p_k^a(\theta; x) := P_k^a(\theta; x) - \bar{P}^a(x)$, respectively. The azimuthal Fourier transform of p^a is defined in the usual manner: $p_k^a(\theta; x) \overset{\mathcal{F}_m}{\mapsto} \hat{p}_k^a(x, m)$. The pressure signals on the linear array are denoted as $P^l\colon \mathbb{R} \times \mathcal{X}_p^l \to \mathbb{R}$ and $P^l\colon (t; x) \mapsto \mathbb{R}$. In discrete time, the notation is $P_k^l(x) \equiv P^l(t = kT_s; x)$. The corresponding time mean and fluctuating quantities are, respectively, $\bar{P}^l(x) := E\{P_k^l(x)\}$ and $p_k^l(x) := P_k^l(x) - \bar{P}^l(x)$. Using the preceding notation, the following output vectors are defined:

$$\hat{\mathbf{p}}_k^a(m) := [\, \hat{p}_k^a(x_1, m) \quad \cdots \quad \hat{p}_k^a(x_{N_p^a}, m)\,]^T \tag{8a}$$

$$\mathbf{p}_k^l := [\, p_k^l(x_1) \quad \cdots \quad p_k^a(x_{N_p^l})\,]^T \tag{8b}$$

Remark 2: Since the jet is axisymmetric, the statistics should be independent of the direction of measurement of the azimuthal coordinate. In [7], this property was invoked to show that, given any realization identified by the set $\{\{\boldsymbol{\alpha}(m)\}_{m=0}^{N_m}, \{\hat{\mathbf{p}}^a(m)\}_{m=0}^{N_m}, \mathbf{p}^l\}$, one can extend the database by appending another realization that is characterized by $\{\{\boldsymbol{\alpha}^*(m)\}_{m=0}^{N_m}, \{\hat{\mathbf{p}}^{a*}(m)\}_{m=0}^{N_m}, \mathbf{p}^l\}$. Following this reasoning, one can conclude that any order of statistical moment involving these quantities would be real, although the individual quantities are complex.

Remark 3: Using the preceding property along with the properties of the Fourier transform, one may derive the following:

$$E\{\hat{p}_k^{a,r}(x,m)\hat{p}_k^{a,r}(x',m)\} = E\{\hat{p}_k^{a,i}(x,m)\hat{p}_k^{a,i}(x',m)\}, \quad m \neq 0 \tag{9a}$$

$$E\{\hat{p}_k^{a,r}(x,m)\hat{p}_k^{a,i}(x',m)\} = 0 \tag{9b}$$

$$\hat{p}_k^a(x,-m) = \hat{p}_k^{a*}(x,m) \tag{9c}$$

Remark 4: Consider K arbitrary scalar fields in the azimuthal Fourier domain $\hat{w}^1(m_1)$ to $\hat{w}^K(m_K)$. Then, their cumulative spectrum satisfies the relation

$$E\{\hat{w}^1(m_1) \times \cdots \times \hat{w}^K(m_K)\} = \hat{\Pi}_{w^1,\cdots,w^K}(m_1, \cdots, m_K)\delta_{m_1+\cdots+m_K,0}$$

In the preceding, $\hat{\Pi}$ is the azimuthal Fourier transform of the corresponding cumulative correlation in the physical domain. In particular, this means that $\hat{w}^K(m_K)$ is only correlated to certain products of azimuthal modes of the remaining variables.

A. Stochastic Estimation

1. Linear Stochastic Estimation

Denote the linear stochastic estimate of $\boldsymbol{\alpha}_k(m)$ given the measurement at time instant k' by $\tilde{\boldsymbol{\alpha}}_{\mathrm{LSE},k\backslash k'}(m)$. Note that the estimate implicitly depends on the choice of $\mathcal{X}_p^a$ and $\mathcal{X}_p^l$. The following linear model is posited for the LSE with time separation due to convection

$$\tilde{\boldsymbol{\alpha}}_{\mathrm{LSE},k+N_c\backslash k}(m) = \mathbf{L}_{\mathrm{LSE}}^{a*}(m, N_c)\hat{\mathbf{p}}_k^a(m) + \mathbf{L}_{\mathrm{LSE}}^{l*}(m, N_c)\mathbf{p}_k^l \tag{10}$$

where $\mathbf{L}_{\mathrm{LSE}}^a \in \mathbb{R}^{N_p^a \times N_n}$ and $\mathbf{L}_{\mathrm{LSE}}^l \in \mathbb{R}^{N_p^l \times N_n}$ represent the families of LSE parameter matrices. Although these parameters are complex in general, it will be shown soon that the axisymmetry of the present problem renders them real. Remark 4 is invoked to argue for the decoupling of the estimation problems for each azimuthal Fourier mode.

LSE proceeds by defining the mean-square estimation error $E\{|\tilde{\alpha}_{\mathrm{LSE},k+N_c\backslash k}^{(n)}(m) - \alpha_{k+N_c}^{(n)}(m)|^2\}$ for each $m-n$ pair, which is quadratic in the respective estimation parameters. The optimal parameter matrix is located at the unique global minimum of the error surface; the expression is

$$\begin{bmatrix} \mathbf{L}_{\mathrm{LSE}}^a(m, N_c) \\ \mathbf{L}_{\mathrm{LSE}}^l(m, N_c) \end{bmatrix} = \begin{bmatrix} E\{\hat{\mathbf{p}}_k^a(m)\hat{\mathbf{p}}_k^{a*}(m)\} & E\{\hat{\mathbf{p}}_k^a(m)\mathbf{p}_k^{l*}\} \\ E\{\mathbf{p}_k^l\hat{\mathbf{p}}_k^{a*}(m)\} & E\{\mathbf{p}_k^l\mathbf{p}_k^{l*}\} \end{bmatrix}^{-1} \times \begin{bmatrix} E\{\hat{\mathbf{p}}_k^a(m)\boldsymbol{\alpha}_{k+N_c}^*(m)\} \\ E\{\mathbf{p}_k^l\boldsymbol{\alpha}_{k+N_c}^*(m)\} \end{bmatrix} \tag{11}$$

Following Remark 2, the estimation parameters can be concluded to be real.

With reference to the preceding formulation, consider how the correlations involving a particular linear array sensor would be modified if it were supplanted by an azimuthal array at the same axial location. Invoking the orthonormality of the Fourier basis, one obtains

$$E\{p_k^l(x)\boldsymbol{\alpha}_{k'}^*(m)\} = E\left\{\sum_{m'=-\infty}^{\infty} \hat{p}_k^a(x,m')e^{im'(\theta=0)}\boldsymbol{\alpha}_{k'}^*(m)\right\} = E\{\hat{p}_k^a(x,m)\boldsymbol{\alpha}_{k'}^*(m)\} \tag{12a}$$

$$E\{p_k^l(x)\hat{\mathbf{p}}_k^{a*}(m)\} = E\{\hat{p}_k^a(x,m)\hat{\mathbf{p}}_k^{a*}(m)\} \tag{12b}$$

$$E\{p_k^l(x)p_k^l(x')\} = \sum_{m=-\infty}^{\infty} E\{\hat{p}_k^a(x,m)\hat{p}_k^{a*}(x',m)\} \tag{12c}$$

The preceding analysis shows that, except for $E\{\mathbf{p}_k^l\mathbf{p}_k^{l*}\}$, all the other terms appearing in Eq. (11) are unchanged if an azimuthal ring array of sensors is used in place of the single sensor on the linear array at the

same axial location. This explains the logic behind a configuration consisting of a combination of linear and azimuthal arrays of sensors, instead of the more expensive arrangement consisting of multiple azimuthal arrays.

2. Quadratic Stochastic Estimation

Denote the quadratic stochastic estimate of $\alpha_k^{(n)}(m)$, given the measurement at time instant k' by $\tilde{\alpha}^{(n)}_{\mathrm{QSE},k\backslash k'}(m)$. Then, the following quadratic model is posited for the QSE with time separation due to convection

$$\begin{aligned}\tilde{\alpha}^{(n)}_{\mathrm{QSE},k+N_c\backslash k}(m) &= \delta_{m,0}c_{\mathrm{QSE}}(n,N_c) + \sum_{s=1}^{N_p^a} l^a_{\mathrm{QSE}}(s,m,n,N_c)\hat{p}^a_k(x_s,m) \\ &+ \sum_{s=1}^{N_p^l} l^l_{\mathrm{QSE}}(s,m,n,N_c)p^l_k(x_s) + \sum_{m'=m-N_m}^{N_m}\sum_{s,s'=1}^{N_p^a}\hat{p}^a_k(x_s,m') \\ &\times q^{aa}_{\mathrm{QSE}}(s,s',m',m-m',n,N_c)\hat{p}^a_k(x_{s'},m-m') \\ &+ \sum_{s,s'=1}^{N_p^l} q^{ll}_{\mathrm{QSE}}(s,s',m,n,N_c)p^l_k(x_s)p^l_k(x_{s'}) \\ &+ \sum_{m'=-N_m}^{N_m}\sum_{s=1}^{N_p^a}\sum_{s'=1}^{N_p^l} q^{al}_{\mathrm{QSE}}(s,s',m',m,n,N_c)\hat{p}^a_k(x_s,m')p^l_k(x_{s'}) \quad (13)\end{aligned}$$

Remark 4 dictates the particular azimuthal modes of pressure retained in the preceding expression, and the estimation parameters can be shown to be real by appealing to Remark 2. The constant term addresses the fact that some of the quadratic terms do not vanish in ensemble averaging of the preceding equation.

A review of the literature did not reveal any exposition of the implementation of QSE for multipoint measurements in a Fourier modal domain. Thus, a sketch of the procedure is provided in the Appendix.

B. Infinite-Impulse Response Filtering

An infinite-impulse response filter uses the predictive capability of a dynamical model of the flow to systematically reduce pass-through of measurement noise to the state estimate. For linear models, the KF is the optimal filter, so that the linearized version of the ROM presented in Eq. (6) is a good starting point. The KF is time varying, so that one has to perform the computations for the filter gains in real time. Since the gains do not depend on the actual measurements, one can also precompute them to reduce processor overhead, with a commensurate increase in memory requirement. If the filter is stable, then the gains reach steady state. Using the steady-state gains in an LTIF may be a viable alternative to the KF. For nonlinear models, such as the ROM in Eq. (6), the extended KF (EKF) is an ad hoc extension of the KF that is known to be suboptimal. All three aforementioned filters are well established [40], and they are implemented in this work. It must be mentioned here that EKF is not the only IIR filter available for nonlinear models. However, the alternatives, such as unscented KF, iterated EKF, and particle filter, are even more computation intensive, and thus deemed unsuitable for the present application.

1. Kalman Filter

In the absence of any further information regarding the specific feedback control scheme, a typical stabilization problem may be assumed, wherein the fluctuations from the mean value are expected to be small. The trivial solution of the ROM in Eq. (6) is an equilibrium point, and it signifies the mean flow. Linearizing about this point involves simply truncating the quadratic portion of the vector field. Note that this decouples the dynamics of the individual azimuthal modes. Previously, it has been pointed out that the filter needs to be implemented in a sampled-data system. Then, the following linearized model is obtained:

$$\boldsymbol{\alpha}_{k+1}(m) = \mathbf{F}(m)\boldsymbol{\alpha}_k(m) + \boldsymbol{\psi}_{\mathrm{KF},k}(m) \quad (14)$$

Here, $\mathbf{F}(m) = \exp(\mathbf{F}^c(m)T_s) \in \mathbb{R}^{N_n\times N_n}$, with $\{\mathbf{F}^c(m)\}_{n,n'} = f_{nn'}(m)$ from Eq. (6) [54]. As is common in filtering, the uncertainties introduced by the modeling approximations, including the linearization, are addressed by the family of additive noise sequences $\boldsymbol{\psi}_{\mathrm{KF}} \in \mathbb{C}^{N_n}$, which are assumed to be stationary independent random processes (white noise) with identically zero-mean and constant covariance matrices

$$E\{\boldsymbol{\psi}_{\mathrm{KF},k}(m)\boldsymbol{\psi}^*_{\mathrm{KF},k'}(m')\} = \boldsymbol{\Psi}_{\mathrm{KF}}(m)\delta_{k,k'}\delta_{m,m'} \quad (15)$$

The symmetric matrices $\boldsymbol{\Psi}_{\mathrm{KF}}$ are real following Remark 2.

Apart from the dynamical model presented, the KF also assumes a linear static map linking the measured output to the state. The following set of output equations specifies the measured pressure as a linear function of the POD modal coefficients with the time separation discussed previously:

$$\hat{\mathbf{p}}^{\,a}_k(m) = \mathbf{L}^{a*}_{\mathrm{KF}}(m,N_c)\boldsymbol{\alpha}_{k+N_c}(m) + \boldsymbol{\xi}^a_{\mathrm{KF},k}(m,N_c) \quad (16a)$$

$$\mathbf{p}^{\,l}_k = \sum_{m=0}^{N_m}\mathbf{L}^{l*}_{\mathrm{KF}}(m,N_c)\boldsymbol{\alpha}^r_{k+N_c}(m) + \boldsymbol{\xi}^l_{\mathrm{KF},k}(N_c) \quad (16b)$$

The linear operators are $\mathbf{L}^a_{\mathrm{KF}} \in \mathbb{R}^{N_n\times N_p^a}$ and $\mathbf{L}^l_{\mathrm{KF}} \in \mathbb{R}^{N_n\times N_p^l}$; more will be said about these. The decoupling of the azimuthal Fourier modes in the first equation follows from Remark 4. The imaginary parts of the POD modal coefficients are absent from the second equation, following the arguments made in Remark 2. The measurement uncertainties are modeled by the families of additive sequences $\boldsymbol{\xi}^a_{\mathrm{KF}} \in \mathbb{C}^{N_p^a}$ and $\boldsymbol{\xi}^l_{\mathrm{KF}} \in \mathbb{R}^{N_p^l}$ that are independent random processes (white noise) with identically zero means and constant covariance matrices

$$E\{\boldsymbol{\xi}^a_{\mathrm{KF},k}(m,N_c)\boldsymbol{\xi}^{a*}_{\mathrm{KF},k'}(m',N_c)\} = \boldsymbol{\Xi}^{aa}_{\mathrm{KF}}(m,N_c)\delta_{k,k'}\delta_{m,m'} \quad (17a)$$

$$E\{\boldsymbol{\xi}^l_{\mathrm{KF},k}(N_c)\boldsymbol{\xi}^{l*}_{\mathrm{KF},k'}(N_c)\} = \boldsymbol{\Xi}^{ll}_{\mathrm{KF}}(N_c)\delta_{k,k'} \quad (17b)$$

$$E\{\boldsymbol{\xi}^a_{\mathrm{KF},k}(m,N_c)\boldsymbol{\xi}^{l*}_{\mathrm{KF},k'}(N_c)\} = \boldsymbol{\Xi}^{al}_{\mathrm{KF}}(m,N_c)\delta_{k,k'} \quad (17c)$$

The covariance matrices are real following Remark 2. Additionally, it is commonplace to assume that the state uncertainties appearing in Eq. (14) are not correlated with the measurement uncertainties; that is,

$$E\{\boldsymbol{\psi}_{\mathrm{KF},k}(m)\boldsymbol{\xi}^{a*}_{\mathrm{KF},k'}(m',N_c)\} = \mathbf{0} \quad (18a)$$

$$E\{\boldsymbol{\psi}_{\mathrm{KF},k}(m)\boldsymbol{\xi}^{l*}_{\mathrm{KF},k'}(N_c)\} = \mathbf{0} \quad (18b)$$

It has been mentioned that the parameter matrices $\mathbf{L}^a_{\mathrm{KF}}$ and $\mathbf{L}^l_{\mathrm{KF}}$ would be determined using SE. Appealing to the orthogonality of the POD modal coefficients from Eq. (4), the LSE yields

$$\begin{aligned}\mathbf{L}^a_{\mathrm{KF}}(m,N_c) &= \begin{bmatrix} \frac{E\left\{\alpha^{(1)}_{k+N_c}(m)\hat{\mathbf{p}}^{a*}_k(m)\right\}}{\Lambda^{(1)}(m)} \\ \vdots \\ \frac{E\left\{\alpha^{(N_n)}_{k+N_c}(m)\hat{\mathbf{p}}^{a*}_k(m)\right\}}{\Lambda^{(N_n)}(m)} \end{bmatrix} \\ \mathbf{L}^l_{\mathrm{KF}}(m,N_c) &= \begin{bmatrix} \frac{2E\left\{\alpha^{(1),r}_{k+N_c}(m)\mathbf{p}^{l*}_k\right\}}{(1+\delta_{m,0})\Lambda^{(1)}(m)} \\ \vdots \\ \frac{2E\left\{\alpha^{(N_n),r}_{k+N_c}(m)\mathbf{p}^{l*}_k\right\}}{(1+\delta_{m,0})\Lambda^{(N_n)}(m)} \end{bmatrix} \end{aligned} \quad (19)$$

The parameter matrices are real following Remark 2.

Now, as in Sec. III.A.1, consider what happens when an azimuthal array of sensors is used in place of a single sensor on the linear array at the same axial location. Using arguments that are similar to those presented in Eq. (12a), along with those made in Remark 1, one can show that

$$E\{\alpha_{k+N_c}^{(n),r}(m)\, p_k^{l*}(x)\} = E\{\alpha_{k+N_c}^{(n)}(m)\, \hat{p}_k^{a*}(x,m)\} \tag{20}$$

This provides a simple relation between the relevant model parameters in Eq. (19).

The new state uncertainty sequence remains a zero-mean independent random process, and its covariance can be derived from Remark 1 and Eq. (15):

$$E\{\breve{\boldsymbol{\psi}}_{\mathrm{KF},k}\breve{\boldsymbol{\psi}}_{\mathrm{KF},k'}^{*}\} := \breve{\boldsymbol{\Psi}}_{\mathrm{KF}}\delta_{k,k'} = \delta_{k,k'} \times \mathrm{diag}\left(\left[\boldsymbol{\Psi}_{\mathrm{KF}}(0)\ \tfrac{1}{2}\boldsymbol{\Psi}_{\mathrm{KF}}(1)\ \cdots\ \tfrac{1}{2}\boldsymbol{\Psi}_{\mathrm{KF}}(N_m)\ \tfrac{1}{2}\boldsymbol{\Psi}_{\mathrm{KF}}(1)\ \cdots\ \tfrac{1}{2}\boldsymbol{\Psi}_{\mathrm{KF}}(N_m)\right]\right)$$

The new measurement uncertainty sequence also remains a zero-mean independent random process, and its covariance can be derived from Remark 3 and Eq. (17):

$$E\{\breve{\boldsymbol{\xi}}_{\mathrm{KF},k}(N_c)\breve{\boldsymbol{\xi}}_{\mathrm{KF},k'}^{*}(N_c)\} =: \breve{\boldsymbol{\Xi}}_{\mathrm{KF}}(N_c)\delta_{k,k'} = \begin{bmatrix} \boldsymbol{\Xi}_{\mathrm{KF}}^{aa}(0) & 0 & \cdots & \cdots & \cdots & \cdots & 0 & \boldsymbol{\Xi}_{\mathrm{KF}}^{al}(0) \\ 0 & \frac{1}{2}\boldsymbol{\Xi}_{\mathrm{KF}}^{aa}(1) & \cdots & 0 & \cdots & \cdots & 0 & \boldsymbol{\Xi}_{\mathrm{KF}}^{al}(1) \\ \vdots & \vdots & \ddots & \vdots & \vdots & \ddots & \vdots & \vdots \\ 0 & 0 & \cdots & \frac{1}{2}\boldsymbol{\Xi}_{\mathrm{KF}}^{aa}(N_m) & 0 & \cdots & 0 & \boldsymbol{\Xi}_{\mathrm{KF}}^{al}(N_m) \\ 0 & \cdots & \cdots & 0 & \frac{1}{2}\boldsymbol{\Xi}_{\mathrm{KF}}^{aa}(1) & \cdots & 0 & 0 \\ \vdots & \vdots & \ddots & \vdots & \vdots & \ddots & \vdots & \vdots \\ 0 & 0 & \cdots & 0 & 0 & \cdots & \frac{1}{2}\boldsymbol{\Xi}_{\mathrm{KF}}^{aa}(N_m) & 0 \\ \boldsymbol{\Xi}_{\mathrm{KF}}^{al*}(0) & \boldsymbol{\Xi}_{\mathrm{KF}}^{al*}(1) & \cdots & \boldsymbol{\Xi}_{\mathrm{KF}}^{al*}(N_m) & 0 & \cdots & 0 & \boldsymbol{\Xi}_{\mathrm{KF}}^{ll} \end{bmatrix}\delta_{k,k'}$$

The output equation (16b) requires partitioning the state vector into real and imaginary parts. It also couples all the azimuthal Fourier modes from the perspective of the filter. In view of this, the accent $(\breve{\cdot})$ is used to indicate the new real quantity formed by assembling all the corresponding complex quantities in the azimuthal Fourier domain as follows:

$$\breve{\boldsymbol{\alpha}}_k := [\{\boldsymbol{\alpha}_k(0)\}^T \quad \{\boldsymbol{\alpha}_k^r(1)\}^T \quad \cdots \quad \{\boldsymbol{\alpha}_k^r(N_m)\}^T \quad \{\boldsymbol{\alpha}_k^i(1)\}^T \quad \cdots \quad \{\boldsymbol{\alpha}_k^i(N_m)\}^T]^T \tag{21a}$$

$$\breve{\mathbf{p}}_k := [\{\hat{\mathbf{p}}_k^a(0)\}^T \quad \{\hat{\mathbf{p}}_k^{a,r}(1)\}^T \quad \cdots \quad \{\hat{\mathbf{p}}_k^{a,r}(N_m)\}^T \quad \{\hat{\mathbf{p}}_k^{a,i}(1)\}^T \quad \cdots \quad \{\hat{\mathbf{p}}_k^{a,i}(N_m)\}^T \quad \{\mathbf{p}_k^l\}^T]^T \tag{21b}$$

$$\breve{\boldsymbol{\psi}}_{\mathrm{KF},k} := [\{\boldsymbol{\psi}_{\mathrm{KF},k}(0)\}^T \quad \{\boldsymbol{\psi}_{\mathrm{KF},k}^r(1)\}^T \quad \cdots \quad \{\boldsymbol{\psi}_{\mathrm{KF},k}^r(N_m)\}^T \quad \{\boldsymbol{\psi}_{\mathrm{KF},k}^i(1)\}^T \quad \cdots \quad \{\boldsymbol{\psi}_{\mathrm{KF},k}^i(N_m)\}^T]^T \tag{21c}$$

$$\breve{\boldsymbol{\xi}}_{\mathrm{KF},k}(N_c) := [\{\boldsymbol{\xi}_{\mathrm{KF},k}^a(0,N_c)\}^T \quad \{\boldsymbol{\xi}_{\mathrm{KF},k}^{a,r}(1,N_c)\}^T \quad \cdots \quad \{\boldsymbol{\xi}_{\mathrm{KF},k}^{a,r}(N_m,N_c)\}^T \quad \{\boldsymbol{\xi}_{\mathrm{KF},k}^{a,i}(1,N_c)\}^T \quad \cdots \quad \{\boldsymbol{\xi}_{\mathrm{KF},k}^{a,i}(N_m,N_c)\}^T \quad \{\boldsymbol{\xi}_{\mathrm{KF},k}^{l}(N_c)\}^T]^T \tag{21d}$$

From Eq. (18), one obtains

$$E\{\breve{\boldsymbol{\psi}}_{\mathrm{KF},k}\breve{\boldsymbol{\xi}}_{\mathrm{KF},k'}^{*}(N_c)\} = \mathbf{0}$$

Then, the model becomes

$$\breve{\boldsymbol{\alpha}}_{k+1} = \breve{\mathbf{F}}\breve{\boldsymbol{\alpha}}_k + \breve{\boldsymbol{\psi}}_{\mathrm{KF},k} \tag{22a}$$

$$\breve{\mathbf{p}}_k = \breve{\mathbf{L}}_{\mathrm{KF}}^T(N_c)\breve{\boldsymbol{\alpha}}_{k+N_c} + \breve{\boldsymbol{\xi}}_{\mathrm{KF},k}(N_c) \tag{22b}$$

Since $\mathbf{F}(m)$ in Eq. (14) is real for all m, the new state-transition matrix is the block-diagonal concatenation

$$\breve{\mathbf{F}} := \mathrm{diag}([\mathbf{F}(0) \quad \mathbf{F}(1) \quad \cdots \quad \mathbf{F}(N_m) \quad \mathbf{F}(1) \quad \cdots \quad \mathbf{F}(N_m)])$$

The form of the new output matrix follows from the modal output matrices in Eq. (16); omitting the functional dependence on N_c for notational convenience, one obtains

$$\breve{\mathbf{L}}_{\mathrm{KF}}(N_c) := \begin{bmatrix} \mathbf{L}_{\mathrm{KF}}^a(0) & 0 & \cdots & 0 & 0 & \cdots & 0 & \mathbf{L}_{\mathrm{KF}}^l(0) \\ 0 & \mathbf{L}_{\mathrm{KF}}^a(1) & \cdots & 0 & 0 & \cdots & 0 & \mathbf{L}_{\mathrm{KF}}^l(1) \\ \vdots & \vdots & \ddots & \vdots & \vdots & \ddots & \vdots & \vdots \\ 0 & 0 & \cdots & \mathbf{L}_{\mathrm{KF}}^a(N_m) & 0 & \cdots & 0 & \mathbf{L}_{\mathrm{KF}}^l(N_m) \\ 0 & 0 & \cdots & 0 & \mathbf{L}_{\mathrm{KF}}^a(1) & \cdots & 0 & 0 \\ \vdots & \vdots & \ddots & \vdots & \vdots & \ddots & \vdots & \vdots \\ 0 & 0 & \cdots & 0 & 0 & \cdots & \mathbf{L}_{\mathrm{KF}}^a(N_m) & 0 \end{bmatrix}$$

Denote the KF estimate of $\breve{\boldsymbol{\alpha}}_k$ given all measurements up to and including instant k' by $\tilde{\breve{\boldsymbol{\alpha}}}_{\mathrm{KF},k/k'}$. Note the difference from the corresponding notation for single-time SE. Let $\boldsymbol{\Theta}_{\mathrm{KF},k/k'}$ be the

autocovariance of the estimation error at k, given the measurements up to k'; that is,

$$\mathbf{\Theta}_{\mathrm{KF},k/k'} := E[\{\tilde{\tilde{\boldsymbol{\alpha}}}_{\mathrm{KF},k/k'} - \breve{\boldsymbol{\alpha}}_k\}\{\tilde{\tilde{\boldsymbol{\alpha}}}_{\mathrm{KF},k/k'} - \breve{\boldsymbol{\alpha}}_k\}^*]$$

Then, the following relations specify the KF [40]:

$$\begin{aligned}\mathbf{K}_{\mathrm{KF},k}(N_c) &= \mathbf{\Theta}_{\mathrm{KF},k+N_c/k-1}\breve{\mathbf{L}}_{\mathrm{KF}}(N_c)(\breve{\mathbf{L}}^T_{\mathrm{KF}}(N_c)\mathbf{\Theta}_{\mathrm{KF},k+N_c/k-1}\breve{\mathbf{L}}_{\mathrm{KF}}(N_c) \\ &\quad + \breve{\mathbf{\Xi}}_{\mathrm{KF}}(N_c))^{-1} \qquad (23a)\end{aligned}$$

$$\begin{aligned}\tilde{\tilde{\boldsymbol{\alpha}}}_{\mathrm{KF},k+N_c/k} &= \tilde{\tilde{\boldsymbol{\alpha}}}_{\mathrm{KF},k+N_c/k-1} \\ &\quad + \mathbf{K}_{\mathrm{KF},k}(N_c)(\breve{\mathbf{p}}_k - \breve{\mathbf{L}}^T_{\mathrm{KF}}(N_c)\tilde{\tilde{\boldsymbol{\alpha}}}_{\mathrm{KF},k+N_c/k-1}) \qquad (23b)\end{aligned}$$

$$\mathbf{\Theta}_{\mathrm{KF},k+N_c/k} = \mathbf{\Theta}_{\mathrm{KF},k+N_c/k-1} - \mathbf{K}_{\mathrm{KF},k}(N_c)\breve{\mathbf{L}}^T_{\mathrm{KF}}(N_c)\mathbf{\Theta}_{\mathrm{KF},k+N_c/k-1} \qquad (23c)$$

$$\tilde{\tilde{\boldsymbol{\alpha}}}_{\mathrm{KF},k+N_c+1/k} = \breve{\mathbf{F}}\tilde{\tilde{\boldsymbol{\alpha}}}_{\mathrm{KF},k+N_c/k} \qquad (23d)$$

$$\mathbf{\Theta}_{\mathrm{KF},k+N_c+1/k} = \breve{\mathbf{F}}\mathbf{\Theta}_{\mathrm{KF},k+N_c/k}\breve{\mathbf{F}}^T + \breve{\mathbf{\Psi}}_{\mathrm{KF}} \qquad (23e)$$

$$\tilde{\tilde{\boldsymbol{\alpha}}}_{\mathrm{KF},k'/-1} = \mathbf{0}, \qquad k' \in [0, N_c] \qquad (23f)$$

$$\mathbf{\Theta}_{\mathrm{KF},k'/-1} = \mathrm{diag}(\Lambda^{(1)}(0) \cdots \Lambda^{(N_n)}(0)\ \tfrac{1}{2}\Lambda^{(1)}(1) \cdots \tfrac{1}{2}\Lambda^{(N_n)}(1) \quad \cdots \tfrac{1}{2}\Lambda^{(1)}(N_m) \cdots \tfrac{1}{2}\Lambda^{(N_n)}(N_m)\ \tfrac{1}{2}\Lambda^{(1)}(1) \cdots \tfrac{1}{2}\Lambda^{(N_n)}(1) \quad \cdots \tfrac{1}{2}\Lambda^{(1)}(N_m) \cdots \tfrac{1}{2}\Lambda^{(N_n)}(N_m)) \quad k' \in [0, N_c] \qquad (23g)$$

The first equation defines the time-varying Kalman gain, the next two define the measurement updates of the state and its error covariance, and the fourth and fifth equations establish their respective time updates. The sixth equation sets the initial condition for the state estimate to the zero vector, in the absence of any other information. Then, the initial condition for the error covariance in the last equation becomes equal to the covariance of the state vector itself; its form is derived from Remark 1.

2. Linear Time-Invariant Filter

The state dynamics and output equations in Eq. (22) are time invariant, but the state model may not have a stable equilibrium. Then, the KF will be asymptotically stable if 1) the pair $[\breve{\mathbf{F}},\ \breve{\mathbf{L}}^T_{\mathrm{KF}}(N_c)]$ is completely detectable; and 2) the pair $[\breve{\mathbf{F}},\ \breve{\mathbf{\Psi}}_1]$ is stabilizable for any $\breve{\mathbf{\Psi}}_1$, such that $\breve{\mathbf{\Psi}}_1\breve{\mathbf{\Psi}}_1^T = \breve{\mathbf{\Psi}}_{\mathrm{KF}}$ (see [40]). The stationary (or steady-state) error-covariance matrix $\mathbf{\Theta}_{\mathrm{LTIF}}(N_c)$ is obtained as the solution of the following discrete-time algebraic Riccati equation:

$$\begin{aligned}\mathbf{\Theta}_{\mathrm{LTIF}}(N_c) &= \breve{\mathbf{F}}\mathbf{\Theta}_{\mathrm{LTIF}}(N_c)\breve{\mathbf{F}}^T \\ &\quad - \breve{\mathbf{F}}\mathbf{\Theta}_{\mathrm{LTIF}}(N_c)\breve{\mathbf{L}}_{\mathrm{KF}}(N_c)(\breve{\mathbf{L}}^T_{\mathrm{KF}}(N_c)\mathbf{\Theta}_{\mathrm{LTIF}}(N_c)\breve{\mathbf{L}}_{\mathrm{KF}}(N_c) \\ &\quad + \breve{\mathbf{\Xi}}_{\mathrm{KF}}(N_c))^{-1}\breve{\mathbf{L}}^T_{\mathrm{KF}}(N_c)\mathbf{\Theta}_{\mathrm{LTIF}}(N_c)\breve{\mathbf{F}}^T + \breve{\mathbf{\Psi}}_{\mathrm{KF}} \qquad (24)\end{aligned}$$

The stationary Kalman gain matrix is obtained by inserting $\mathbf{\Theta}_{\mathrm{LTIF}}(N_c)$ in Eq. (23a). Use of a stationary gain reduces the original time-varying KF to the LTIF. Then, the only expressions to be evaluated in real time are Eqs. (23b) and (23d), which makes the LTIF comparable in complexity to the LSE model in Eq. (10).

3. Extended Kalman Filter

The conversion of the continuous ODE with quadratic nonlinearity in Eq. (6) to an equivalent difference equation for a sampled-data system is not obvious. The approach taken here treats the linear part as if the quadratic part were absent, so that the linear part of the difference equation is identical to that in Eq. (14). Subsequently, the quadratic part is determined as if the state derivative were approximated by a first-order forward difference scheme. The resultant state model is the following set of difference equations with quadratic nonlinearity:

$$\begin{aligned}\alpha^{(n)}_{k+1}(m) &= \mathbf{f}_n(m)\boldsymbol{\alpha}_k(m) + \sum_{m'=m-N_m}^{N_m}\{\boldsymbol{\alpha}_k(m')\}^T\mathbf{G}_n(m', m-m') \\ &\quad \times \boldsymbol{\alpha}_k(m-m') + \psi^{(n)}_{\mathrm{EKF},k}(m) \qquad (25)\end{aligned}$$

Here, $\mathbf{f}_n(m)$ is the nth row of $\mathbf{F}(m)$ introduced in Eq. (14), and

$$\{\mathbf{G}_n(m', m-m')\}_{n',n''} = T_s g_{nn'n''}(m', m-m')$$

from Eq. (6). The state uncertainty sequences ψ_{EKF} are modeled in a manner akin to the KF; the details are omitted for brevity.

For the EKF, the output equations are also assumed to be quadratic. Then, the arguments in Remark 4, along with the time separation discussed previously, yield the following model:

$$\begin{aligned}\hat{p}^a_k(x_s, m) &= \delta_{m,0}c^a_{\mathrm{EKF}}(s, N_c) + \sum_{n=1}^{N_n} l^a_{\mathrm{EKF}}(n, m, s, N_c)\alpha^{(n)}_{k+N_c}(m) \\ &\quad + \sum_{m'=m-N_m}^{N_m}\sum_{n,n'=1}^{N_n} q^a_{\mathrm{EKF}}(n, n', m', m-m', s, N_c) \\ &\quad \times \alpha^{(n)}_{k+N_c}(m')\alpha^{(n')}_{k+N_c}(m-m') + \xi^a_{\mathrm{EKF},k}(m, x_s, N_c) \qquad (26a)\end{aligned}$$

$$\begin{aligned}p^l_k(x_s) &= c^l_{\mathrm{EKF}}(s, N_c) + \sum_{m'=-N_m}^{N_m}\sum_{n=1}^{N_n} l^l_{\mathrm{EKF}}(n, m', s, N_c)\alpha^{(n)}_{k+N_c}(m') \\ &\quad + \sum_{m',m''=-N_m}^{N_m}\sum_{n,n'=1}^{N_n} q^l_{\mathrm{EKF}}(n, n', m', m'', s, N_c)\alpha^{(n)}_{k+N_c}(m')\alpha^{(n')}_{k+N_c}(m'') \\ &\quad + \xi^l_{\mathrm{EKF},k}(x_s, N_c) \qquad (26b)\end{aligned}$$

The family of measurement uncertainty sequences ξ^a_{EKF} and ξ^l_{EKF} are modeled in a manner akin to the KF; the details are omitted for brevity. The model in Eq. (26a) can be seen as a special case of the model structure introduced in Eq. (13); the procedure to determine its parameters using QSE is presented in the Appendix. The model in Eq. (26b) can also be analyzed in a similar manner to determine its parameters using QSE. All the parameters of both models are real from arguments in Remark 2.

Following the procedure used for KF, the preceding models can be reduced to the standard form in the real domain. Subsequent to this, the theory of EKF [40] can be applied directly; the details are omitted.

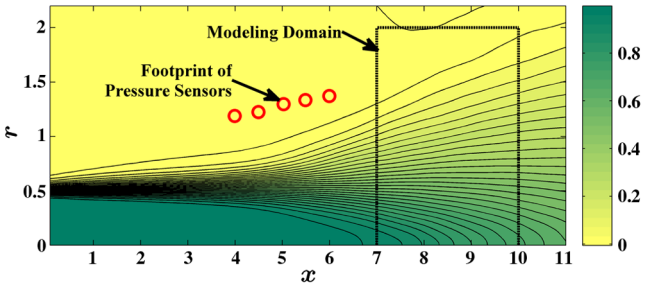

Fig. 2 Meridional half-slice of jet shear layer showing contour plot of mean axial velocity from DNS database. Cross section of cylindrical modeling domain is indicated, and footprints of pressure sensors (azimuthal array or linear array) are depicted.

IV. Results

The details of the DNS database of the Mach 0.9, $Re = 3600$ axisymmetric jet are established in [8]; here, only the most pertinent aspects are highlighted. The original data of the DNS had been saved at 2316 consecutive time instants, with the snapshots having a uniform separation of $T_s = 0.071D/U_{\text{jet}}$. A contour plot of the mean axial velocity is shown in Fig. 2. The low-Re simulated jet remains laminar for a significant length, and its potential core ends at $x \approx 7$ (see [8]). The choice of the vicinity of the end of the potential core as the modeling domain has been explained in Sec. II. In [7], the authors presented a 30-state POD-GP ROM of the velocity field in the cylindrical region indicated in Fig. 2. The 30 states comprised POD modes from 1 through 5 and azimuthal Fourier modes from 0 to 5; thus, $N_n = N_m = 5$.

Figure 3a shows the energies of the POD modal coefficients, which are directly related to the corresponding eigenvalues [7]. This figure clearly shows the low-dimensional nature of the velocity field. Unlike the eigenvalues, the POD modal energies for $m = 0$ are not monotonically decreasing with n, owing to insufficient convergence at the lower energies. The POD was performed using every alternate snapshot indexed from 700 to 1398 out of the total of 2316 snapshots in the database. Figure 3b presents the power spectral density (PSD) of the first POD mode for various azimuthal modes. These were computed with the Welch spectrogram technique using a window size of 400 samples, overlaps of 300 samples, and Hanning windowing [55]. The spectra for $m = 0$ and 1 have definite broadband peaks that are missing for the other azimuthal modes. The corresponding eigenfunctions were presented in [7]; these showed large-scale structures in the potential core and near the high-speed side of the shear layer for $m = 0$ and 1, respectively, whereas the other modes displayed structures in the center and low-speed side of the shear layer. The differences in their spectral character can then be understood from the local velocity spectra observed at these different radial locations in axisymmetric jets by previous researchers [56–60].

The feedback control strategies that are the ultimate goal of this research will subsequently be tested on a Mach 0.9, $Re = 630,000$ laboratory jet with $D = 0.0254$ m. The boundary layer at the nozzle exit has been established to be turbulent, the shear layer of the jet transitions to turbulent in a very short distance from the nozzle exit, and its potential core ends at $x \approx 5.5$ (see [61]). The appropriate axial extent of the modeling domain for this jet would be from $x = 5$ to 8, so as to cover the dynamically interesting region of the shear layer. For real-time estimation of the state of this jet, pressure sensors would be placed between $x = 2$ and 4. Such a configuration would be physically implementable in experiments while ensuring that the feedback controller thus developed would be practically meaningful. The need to obtain a hydrodynamic signature dictates that the sensors be radially located just outside the shear layer [13,15,17]. With this motivation in mind, the numerical experiments reported herein were conducted with virtual pressure sensors placed on a linear array between $x = 4$ and 6 at intervals of 0.5, as shown in Fig. 2. The array makes an angle of 5.6° with the jet axis to parallel the outer edge of the shear layer, with the most upstream sensor located at $r = 1.2$. Alternatively, any or all of the sensors could be replaced by uniform azimuthal arrays of 16 sensors each (of the form shown in Fig. 1). The precise locations of the sensors coincided with the nearest point on the nonuniform DNS grid. The results reported were not altered when all 80 azimuthal points in the computational grid were instrumented instead of just 16 of them, thereby attesting to the convergence of the low-order azimuthal modes.

Figure 3c presents the energies in the various azimuthal modes of pressure measured on the ring arrays discussed. The figure demonstrates the familiar low-dimensional character of the pressure field, as well as the downstream energy growth, that has been observed by previous researchers [17,60,62,63]. These works have also

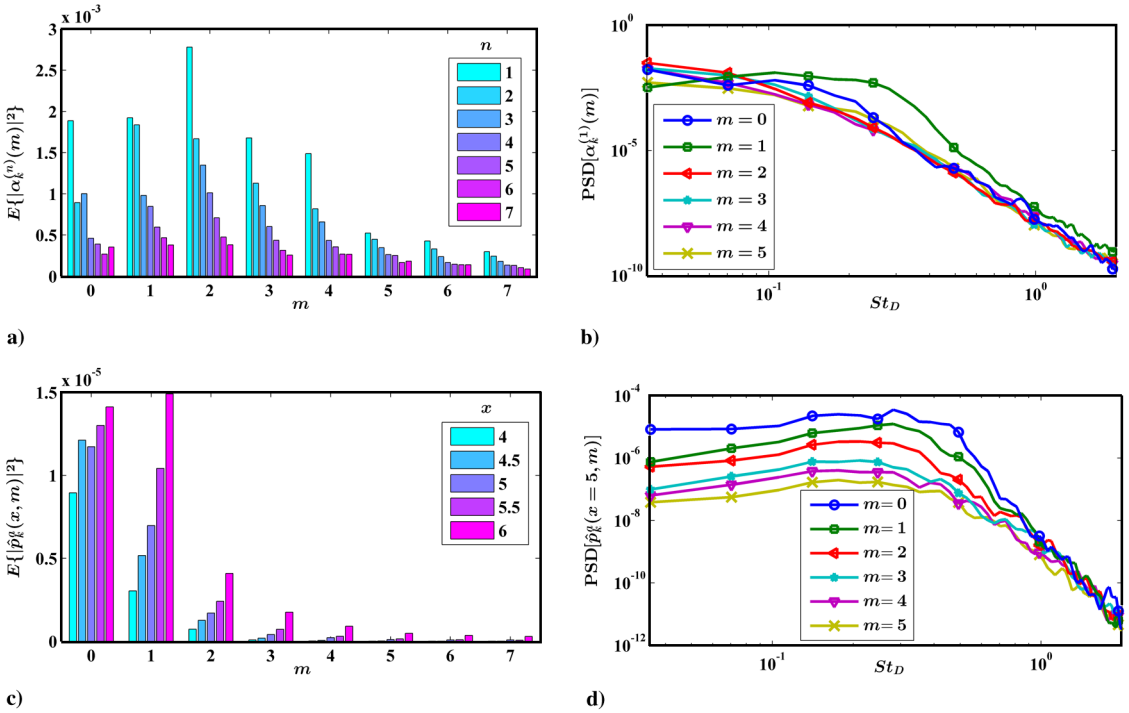

Fig. 3 Lower Fourier azimuthal modes: a) variance of leading-order POD modes, b) PSD of first POD modes, c) variance of near-field pressure measured at several axial stations, and d) PSD of pressure at $x = 5$. Strouhal number based on jet exit diameter is St_D.

highlighted the differences in the azimuthal modal makeup of pressure and velocity that are clear from a comparison with Fig. 3a. The PSD of the various azimuthal modes of pressure measured at $x = 5$ are shown in Fig. 3d; these were computed using the spectrogram parameters mentioned. Similar pressure spectra were reported in [6] for a ring array of pressure sensors placed at $x = 3$ and $r = 1$ in the experimental jet mentioned.

The temporal order of the snapshots was randomized before dividing them equally into two mutually exclusive sets. The various estimation models discussed in Sec. III were built using the statistics educed from the first set (the training set). The fidelity of each estimation strategy was then tested using the second set (the validation set). While this division into training and validation data sets is ideal for SE, the IIR filters require the entire time history of the output, so that the distinction is not as well defined. The IIR filter models were developed solely from the training set, but they were simulated using the time-resolved pressure from the entire database. Finally, the samples corresponding to the validation data set were selected to evaluate the performance.

To compare the overall performance of the various state estimators, the following modal estimation error metric is established:

$$\eta(n, m, N_c) := \sqrt{\frac{E\{|\tilde{\alpha}^{(n)}_{k+N_c/k}(m) - \alpha^{(n)}_{k+N_c}(m)|^2\}}{\sqrt{E\{|\tilde{\alpha}^{(n)}_{k+N_c/k}(m)|^2\}E\{|\alpha^{(n)}_{k}(m)|^2\}}}} \tag{27}$$

The metric implicitly depends on the choice of the pressure measurement configuration characterized by $\mathcal{X}^a_p$ and $\mathcal{X}^l_p$, as well as the estimation strategy. In fact, the particular estimation strategy is omitted from the subscript for generality. Moreover, the notation appears specific to infinite-memory filters, but it is also applicable to single-time stochastic estimators. A value of η close to 0 indicates high fidelity. The metric will have a moderate value if the instantaneous estimation is not accurate, but the variance of the state α is well replicated by the estimate. On the other hand, η will become large whenever the variance of the estimate is significantly disparate from that of the state. A more concise but less informative metric is the following global estimation error metric:

$$\breve{\eta}(N_c) := \sqrt{\frac{\sum_{n=1}^{N_n}\sum_{m=-N_m}^{N_m} E\{|\tilde{\alpha}^{(n)}_{k+N_c/k}(m) - \alpha^{(n)}_{k+N_c}(m)|^2\}}{\sqrt{\sum_{n=1}^{N_n}\sum_{m=-N_m}^{N_m} E\{|\tilde{\alpha}^{(n)}_{k+N_c/k}(m)|^2\}\sum_{n=1}^{N_n}\sum_{m=-N_m}^{N_m} E\{|\alpha^{(n)}_{k}(m)|^2\}}}} \tag{28}$$

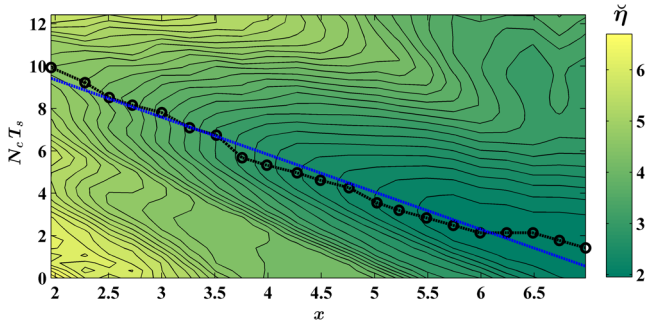

Fig. 4 Estimation error using LSE for various axial locations of the sole azimuthal array of pressure sensors and time separations. Markers trace bottom of error valley, and straight line is best fit through them.

Owing to the orthonormality of the POD and azimuthal Fourier bases, the preceding metric actually represents the estimation error of the physical velocity field.

The convection inherent in the jet results in the pressure signal leading the POD modal coefficient by the time separation that is denoted herein by $N_c T_s$. Although the pressure measurement is localized, the POD modal coefficient is nonlocal. So N_c cannot be directly obtained from the convective velocity of the jet. The approach taken here uses LSE in conjunction with a single azimuthal ring array of sensors to determine the N_c that minimizes $\breve{\eta}$. Figure 4 shows that the curve tracing the bottom of the error valley for each axial location is very well approximated by a line with slope -1.75 and x intercept of 7.3. Because of the implicit normalizations, the negative reciprocal of the slope signifies the ratio of the convective velocity to the jet exit velocity, which is close to the value of 0.6 reported for the original DNS database [8]. The x intercept signifies the apparent centroid of the modeling domain (from $x = 7$ to 10), as represented by its POD basis. The pressure sensing configuration that is chosen for further investigation is centered on $x = 5$, for which the optimal N_c turns out to be 55. This value is used in all further analyses reported, unless otherwise mentioned. It is worth noting that, in similar assays using QSE and LTIF, the same optimal N_c was found.

The coefficients of the ROM presented in Eq. (6) have been determined previously in [7], so that the linear or quadratic state-transition operators appearing in Eqs. (22a) and (25) can be computed. It is noted here that the trivial equilibrium point of the ROM, representing the mean flow, was found to be unstable. This is to be expected, since the actual jet never converges to the mean velocity field. The DNS database is time resolved, so that realizations of the respective modeling uncertainty sequences $\breve{\psi}_{\mathrm{KF}}$ and $\breve{\psi}_{\mathrm{EKF}}$ are directly available. Then, using the white-noise assumption, the corresponding state uncertainty covariances $\breve{\mathbf{\Psi}}_{\mathrm{KF}}$ and $\breve{\mathbf{\Psi}}_{\mathrm{EKF}}$ can be ascertained empirically by ensemble averaging. For this step, each snapshot k had to be paired with the corresponding $k + 1$ snapshot; there were 575 such pairs in the training data set, which was enough for convergence. It must be noted here that the requisite time-resolved empirical velocity database may be educed from

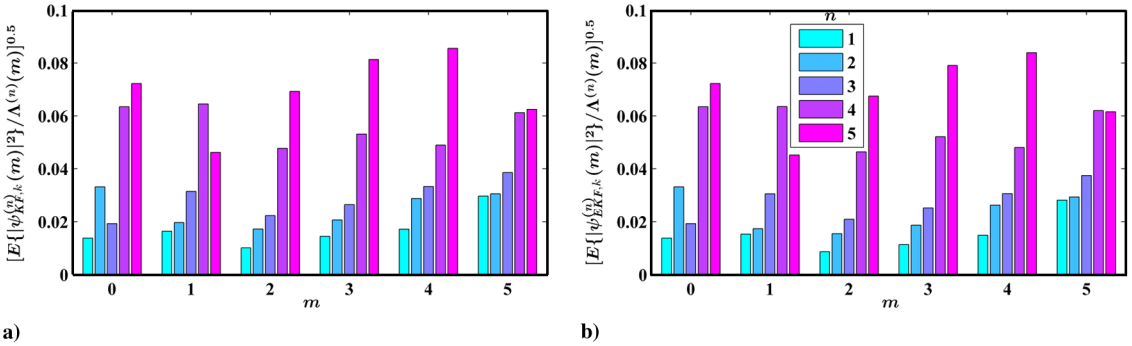

Fig. 5 Normalized standard deviations of state uncertainty sequences for a) KF and b) EKF.

experiments with the modeling strategy adopted in [7], following [17,64]. The diagonal terms of the covariance matrices are shown in Fig. 5; the offdiagonal terms were found to be substantially smaller by comparison. It is interesting to note that, although the quadratic terms are known to be crucial for the correct simulation of the ROM [11], they do not have much effect on the modeling uncertainty.

The next focus is on the linear output relation for the KF appearing in Eq. (16). Recall from Eq. (19) that the model coefficients are to be determined by an application of LSE to the empirical data. This warrants a study of the following set of normalized cross-correlation coefficients

$$\zeta^a_{\alpha p}(n,m,x,N_c) := \frac{E\{\alpha^{(n)}_{k+N_c}(m)\,\hat{p}^{a*}_k(x,m)\}}{\sqrt{\Lambda^{(n)}(m)E\{|\hat{p}^a_k(x,m)|^2\}}} \tag{29a}$$

$$\zeta^l_{\alpha p}(n,m,x,N_c) := \frac{E\{\alpha^{(n)}_{k+N_c}(m)\,p^l_k(x)\}}{\sqrt{\Lambda^{(n)}(m)E\{|p^l_k(x)|^2\}}} \tag{29b}$$

Here, Eq. (4) is invoked to make the substitution $\Lambda^{(n)}(m)=E\{|\alpha^{(n)}_k(m)|^2\}$. The cross-correlation coefficients are real following Remark 2, and their mutual relationship has been established in Eq. (12). The preceding statistics are also relevant to the direct LSE model in Eqs. (10) and (11), which is a dual of the KF output relation.

The convergence of the preceding statistics was assessed for the DNS database. In particular, the correlation coefficients were evaluated from the training data set, as well as from the full database, and the differences were found to be insignificant. In Figs. 6a and 6b, the absolute values of $\zeta^a_{\alpha p}$ and $\zeta^l_{\alpha p}$ are plotted for selected axial locations of the pressure sensors. This should be analyzed from two perspectives. In determining the accuracy of the KF output relation [Eq. (16a)] for a particular $x-m$ combination, one is seeking a high correlation level for any n. Similarly, the relation Eq. (16b) will be accurate for a particular axial location if the correlation level is high for any $m-n$ combination. From this perspective, the linear output equations appear to be feasible. However, the ultimate goal is to observe the model states from the pressure, so that one is seeking high correlation levels for all states. From this perspective, one can conclude that direct LSE would perform poorly if used with a single azimuthal ring array, although additional measurements from the linear array sensors should improve the accuracy of estimation. Since the KF uses an approximate knowledge of the dynamic coupling of the different states in addition to the static output relation, it may be expected to perform better, even with the single ring array of sensors.

A similar study can be made of the third-order moments involved in the direct QSE in Eq. (13), as well as the QSE that determines the quadratic output equation for the EKF in Eq. (26). The relevant normalized correlation coefficients are

$$\zeta^a_{\alpha\alpha p}(n,n',m,m',x,N_c) := \frac{E\{\alpha^{(n)}_{k+N_c}(m')\alpha^{(n')}_{k+N_c}(m-m')\,\hat{p}^{a*}_k(x,m)\}}{\sqrt{\Lambda^{(n)}(m')\Lambda^{(n')}(m-m')E\{|\hat{p}^a_k(x,m)|^2\}}} \tag{30a}$$

$$\zeta^l_{\alpha\alpha p}(n,n',m,m',x,N_c) := \frac{E\{\alpha^{(n)}_{k+N_c}(m)\alpha^{(n')}_{k+N_c}(m')\,\hat{p}^l_k(x)\}}{\sqrt{\Lambda^{(n)}(m)\Lambda^{(n')}(m')E\{|\hat{p}^l_k(x)|^2\}}} \tag{30b}$$

These statistics are real following Remark 2. In Figs. 6c and 6d, the absolute values of some $\zeta^a_{\alpha\alpha p}$ and $\zeta^l_{\alpha\alpha p}$ are depicted. These third-order moments are not insignificant compared with the second-order moments. Thus, a quadratic model can be expected to be more accurate than a linear one. It must be noted that these third-order statistics were not well converged, the consequences of which will be discussed further.

The training data set that was used to determine the coefficients of the output equations (16) and (26) through SE was reused to obtain a realization of the set of corresponding measurement uncertainty sequences ξ^a_{KF}, ξ^l_{KF}, ξ^a_{EKF}, and ξ^l_{EKF}. Then, with the white-noise assumption, the respective measurement uncertainty covariances $\breve{\mathbf{\Xi}}_{\mathrm{KF}}$ and $\breve{\mathbf{\Xi}}_{\mathrm{EKF}}$ were ascertained empirically by ensemble averaging. As an aside, note that for converged statistics, the KF model affords the following simplifications:

$$\frac{E\{|\xi^a_{\mathrm{KF},k}(x,m,N_c)|^2\}}{E\{|\hat{p}^a_k(x,m)|^2\}} = 1-\sum_{n=1}^{N_n}|\zeta^a_{\alpha p}(n,m,x,N_c)|^2,$$

$$\frac{E\{|\xi^l_{\mathrm{KF},k}(x,N_c)|^2\}}{E\{|p^l_k(x)|^2\}} = 1-\sum_{n=1}^{N_n}\sum_{m=-N_m}^{N_m}|\zeta^l_{\alpha p}(n,m,x,N_c)|^2$$

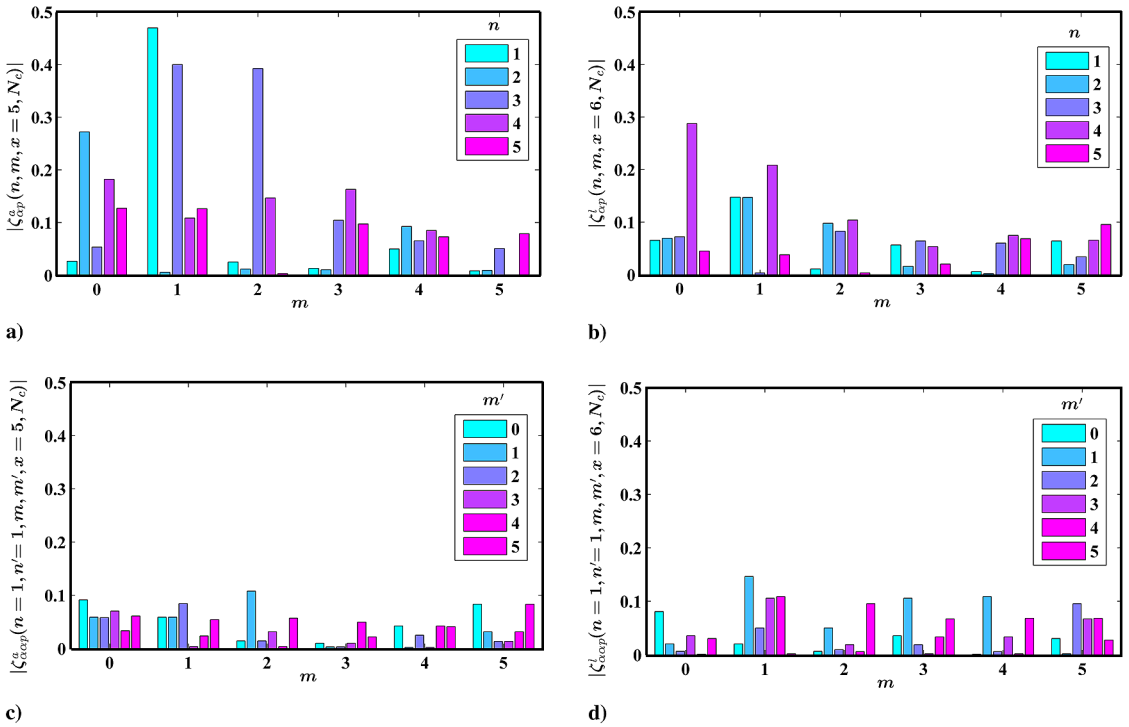

Fig. 6 Normalized second- and third-order correlations of POD modal coefficients with pressure measured in selected configurations, as noted on respective ordinate labels.

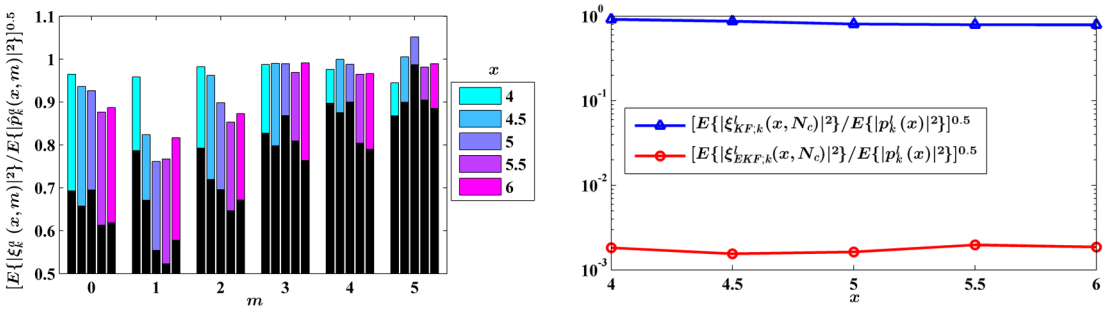

Fig. 7 Normalized standard deviations of measurement uncertainties in KF and EKF models for pressure measured on a) azimuthal array and b) linear array. In Fig. 7a, black bars for EKF are overlaid on the corresponding bars for KF.

This arises due to the least-squares formulation for determining the estimation parameters, as well as the orthonormality of the POD and Fourier bases.

The diagonal terms of the covariance matrices are shown in Fig. 7. Unlike the state uncertainty covariances presented in Fig. 5, the measurement uncertainty covariances are substantially reduced in going from a linear expression to a quadratic one. In assessing these results, it must be borne in mind that the linear output equation for the azimuthal modal pressure measured on a ring array has five parameters to fit the empirical data set of 1131 snapshots. On the other hand, the corresponding quadratic output equation has anywhere from 80 (for $m = 5$) to 146 (for $m = 0$) independent parameters. For the linear array measurements, the linear model has 30 degrees of freedom, whereas the quadratic model has 821. Thus, although the EKF is in principle more accurate than the KF, this profusion of model parameters for the EKF would make it prohibitively expensive for real-time implementation. The large number of model parameters also complicates their determination, owing to poor convergence of the third-order statistics involved. Recalling that the convective time separation $N_c T_s$ was optimized for the azimuthal array of pressure sensors at $x = 5$, it is noteworthy that the output uncertainties are not necessarily minimum at this location.

Recall that at each of the five axial locations considered herein, one could either place a ring array of pressure sensors or a single sensor that belongs to the linear array. All the 242 possible permutations and combinations of measurement configurations were analyzed with each of the estimation strategies presented herein. Table 1 presents the global estimation errors evaluated using the validation data set for the most pertinent and interesting configurations. Based on these results, the following remarks are in order.

1) First, the blanks in the table will be explained. In the case of a QSE with five ring arrays, the covariance matrix of the 96-dimensional regressor for $m = 0$ was close to singularity, so that the estimation parameters could not be determined reliably. This shows that the five ring arrays are unable to provide enough independent information. In the case of an LTIF with five linear array sensors, the detectability criterion mentioned in Sec. III.B.2 was not satisfied, so that the discrete-time algebraic Riccati equation did not have a finite solution. Since the filter stability conditions are sufficient but not necessary, it is not surprising that the KF still gave good results in this case. The filter stability criteria were satisfied in all configurations involving at least one ring array.

2) With the preceding caveat, the performance of the LTIF is seen to be indistinguishable from that of the KF, as long as the ring array is placed at the axial location for which the convective time separation was optimized (i.e., $x = 5$). It will be shown that the equality of the error metric for KF and LTIF is not an artifact of averaging the error over a large number of realizations.

3) The linear IIR filters display only a slight improvement when a linear array of sensors is included in the configuration, and the number of such sensors is seen to be inconsequential. This indicates that the use of the ROM is rendering the additional measurements somewhat redundant.

4) To analyze the degradation of performance of the linear IIR filters in going from cases 5 to 6, the convective time separation $N_c T_s$ was reoptimized for $x = 6$. The new value of $N_c = 33$ (see Fig. 4), when used with configuration 6, yielded $\breve{\eta} = 1.31$ for both KF and LTIF, and $\breve{\eta} = 1.28$ for QSE.

5) Linear IIR filtering matches or outperforms QSE while having substantially reduced real-time computational overhead.

6) The worst performance in all configurations is found with LSE, while QSE represents a large improvement over LSE.

7) The LSE and QSE continue to show significant performance improvements with increasing numbers of measurements.

8) The EKF does not necessarily represent an improvement in performance over the KF. This is most likely a result of improper tuning of the uncertainty covariances resulting from the overfitting of the training data set, as mentioned before. It is also apparent in the inconsistent improvement of fidelity of the EKF with increasing measurement locations. However, the EKF also demonstrates the best performance in the table, viz., in the configuration with five ring arrays.

From the point of view of estimation accuracy and feasibility of implementation, the measurement configuration $\mathcal{X}_p^a = \{5\}$, $\mathcal{X}_p^l = \{4, 4.5, 5.5, 6\}$ is selected for further study based on the preceding discussion. To gain a more intuitive understanding of the behavior of the various estimators in this setup, the trajectories of two estimated states are shown in Fig. 8. The following comments are based on these results.

1) In Fig. 3b, the first POD modal coefficients for $m = 0$ and 1 were shown to have different peak frequencies. This disparity is reflected well in Fig. 8. All the azimuthal modes of pressure demonstrated similar spectral shapes in Fig. 3d. This shape was replicated solely by the $m = 1$, $n = 1$ POD modal coefficient in Fig. 3b. In multipoint LSE performed in the physical domain, the estimated quantity, irrespective of its true spectrum, will have the same spectral shape as the measured quantity [29]. The same argument can be extended to multipoint LSE performed in a spatial Fourier domain when all the independent measurements have similar spectral shapes, as is the present case. This explains the frequency mismatch of the LSE trajectory for $m = 0$, when compared with the true trajectory. It also explains the matching of frequencies and consequent improved

Table 1 Global estimation error $\breve{\eta}$ for all strategies in several measurement configurations

No.	Configuration	Method				
		LSE	QSE	KF	LTIF	EKF
1	$\mathcal{X}_p^a = \emptyset$, $\mathcal{X}_p^l = \{4, 4.5, 5, 5.5, 6\}$	2.52	1.81	1.34	—	1.42
2	$\mathcal{X}_p^a = \{5\}$, $\mathcal{X}_p^l = \emptyset$	2.26	1.88	1.38	1.38	1.43
3	$\mathcal{X}_p^a = \{5\}$, $\mathcal{X}_p^l = \{6\}$	2.16	1.64	1.35	1.35	1.50
4	$\mathcal{X}_p^a = \{5\}$, $\mathcal{X}_p^l = \{4.5, 5.5\}$	2.11	1.51	1.33	1.33	1.42
5	$\mathcal{X}_p^a = \{5\}$, $\mathcal{X}_p^l = \{4, 4.5, 5.5, 6\}$	2.03	1.32	1.32	1.32	1.37
6	$\mathcal{X}_p^a = \{6\}$, $\mathcal{X}_p^l = \{4, 4.5, 5, 5.5\}$	2.00	1.31	1.74	1.93	1.34
7	$\mathcal{X}_p^a = \{4, 4.5, 5, 5.5, 6\}$, $\mathcal{X}_p^l = \emptyset$	1.60	——	1.33	1.32	1.18

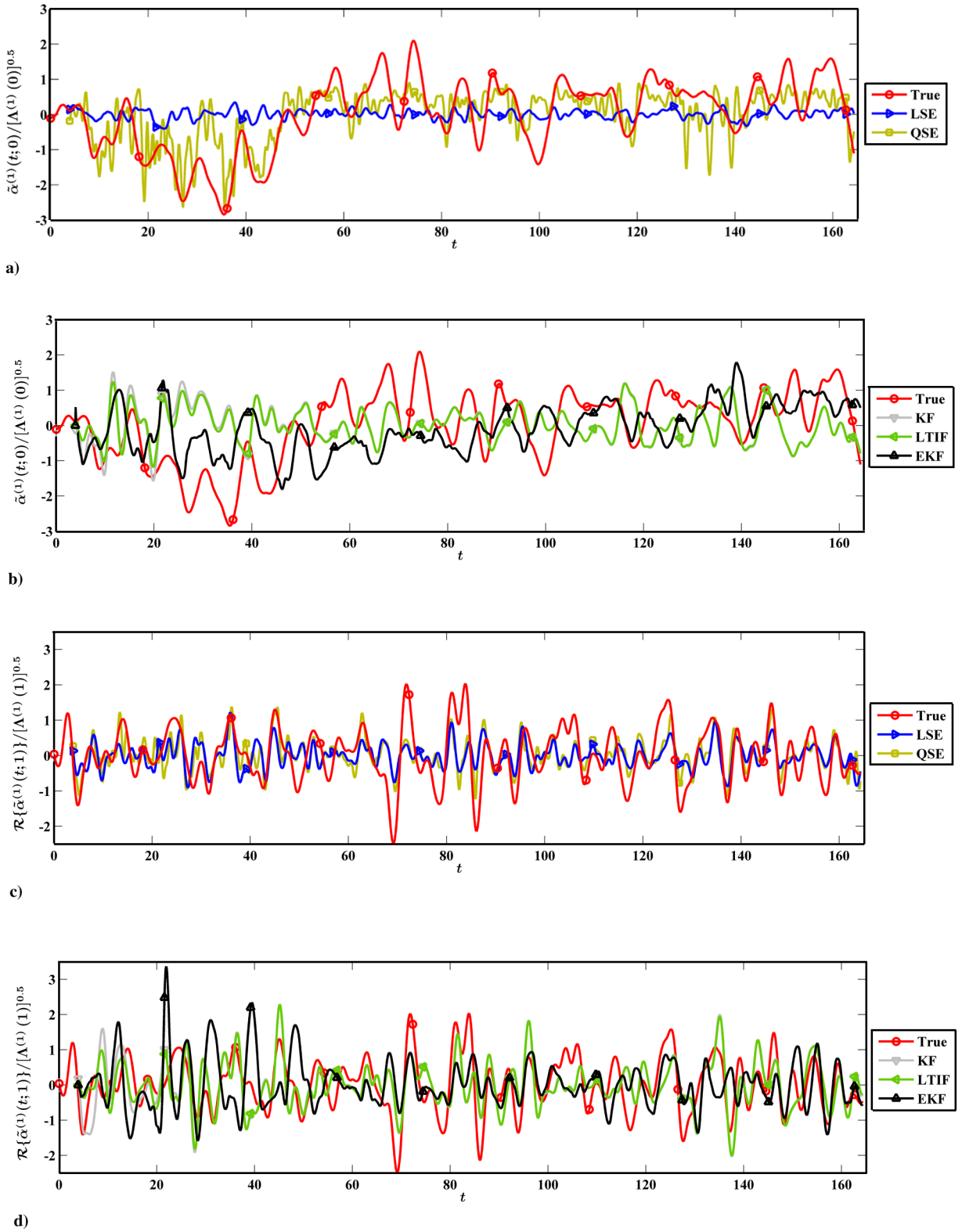

Fig. 8 Trajectories of selected states (as noted on individual ordinate labels) estimated with various strategies in $\mathcal{X}_p^a = \{5\}$, $\mathcal{X}_p^l = \{4, 4.5, 5.5, 6\}$ configuration.

estimation in the $m = 1$ case. The state trajectories estimated by the linear IIR filters have improved frequency matching for both modes owing to their reliance on the ROM, which approximately captures the true frequency content of the state.

2) The KF gains were found to reach steady state within ≈25 flow time steps, and this is borne out by the quick coalescence of the trajectories estimated with KF and LTIF. Moreover, one filter cannot be said to be more accurate than the other during the period that they produced different estimates.

3) The fidelity of KF and EKF cannot be distinguished, in spite of the order-of-magnitude increase in computational complexity in the latter.

4) The LSE essentially gives a null result for $m = 0$, which could have been predicted from the low value of the corresponding correlation coefficient presented in Fig. 6a. The LTIF demonstrates superior fidelity while using the same correlation, since it additionally exploits the knowledge of the dynamic coupling of the states.

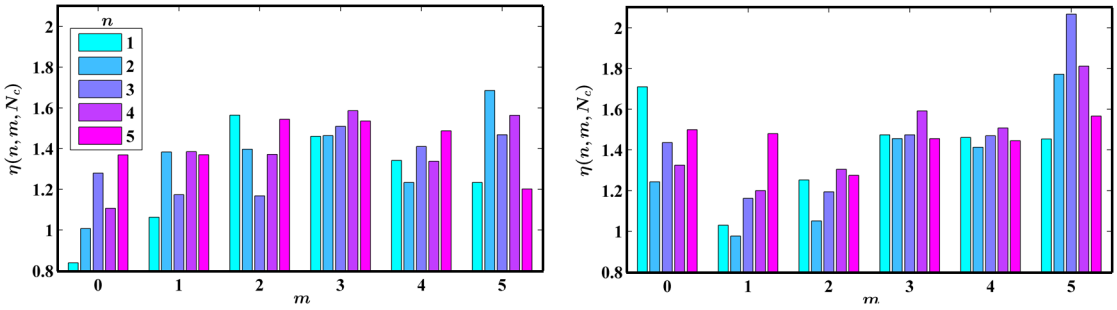

Fig. 9 Modal estimation errors in configuration $\mathcal{X}_p^a = \{5\}$, $\mathcal{X}_p^l = \{4, 4.5, 5.5, 6\}$ using a) QSE and b) LTIF.

5) Compared with LSE, use of QSE significantly improves the estimation performance in the instance of $m = 0$, with an attendant increase in computational cost. However, in the $m = 1$ case, QSE does not demonstrate any obvious improvement over LSE.

The foregoing discussion makes it apparent that the LTIF stands out from the other strategies in terms of estimation accuracy combined with feasibility of real-time implementation. To make this determination more conclusive, a final detailed comparison is made with QSE. The discussion based on Fig. 8 gave some insight, but it was somewhat anecdotal, since only two of the 30 states were considered. For quantitative analysis, the modal estimation error metric η defined in Eq. (27) was evaluated using the validation data set. The results are presented in Fig. 9. Recalling the modal energy spectrum presented in Fig. 3a, it is observed that LTIF generally displays greater accuracy for the more energetic modes. The same cannot be said of QSE. However, the two strategies yield an overall similarity of error levels that could be anticipated from Table 1.

In the Introduction, mention was made of multitime SE as an intermediate between single-time SE and IIR filtering. So it is pertinent to query if multitime LSE can be as effective as LTIF. Multitime QSE need not be considered, because single-time QSE itself poses real-time processing challenges. A multitime LSE was implemented for the measurement configuration $\mathcal{X}_p^a = \{5\}$, $\mathcal{X}_p^l = \{4, 4.5, 5.5, 6\}$, with the same convective time separation as before. It must be noted that owing to the moving window scheme, the training data set was made up of the first half of the database and the validation data set comprised the second half. It was found that a moving window stretching back in time by 25 samples yielded $\breve{\eta} = 1.62$, whereas the best result ($\breve{\eta} = 1.30$) was obtained with a window of 120 samples. The existence of an optimal window size has been demonstrated before [37]. Evidently, the memory requirements of any effective multitime LSE strategy would render it infeasible for real-time estimation.

V. Conclusions

As in many engineering problems, real-time state estimation for feedback flow control poses an essential dilemma between simplicity and performance. Single-time linear and quadratic stochastic estimators have long been the preferred strategy due to their simplicity. At heart, these are essentially curve-fitting techniques that do not exploit any available knowledge of the flow dynamics. Multitime stochastic estimators do incorporate some notion of the dynamics but at the cost of increased memory overhead. A major shortcoming of stochastic estimators is that they pass measurement noise unfiltered to the state estimate. Moreover, some flow states may not have a direct static relation with the measured output, but they may only be observable indirectly through coupled dynamics.

In some cases, a linear time-invariant ROM of the flow dynamics may be at hand. Then a linear time-invariant infinite-memory filter may yield an improved estimation with minimal increase in runtime complexity over the single-time linear stochastic estimator. The two shortcomings of stochastic estimators mentioned may both be mitigated by this technique. The infinite memory of the filter is the result of a recursive update strategy for the state estimate that requires only the previous estimate to be actually held in memory. A time-invariant filter may suffer from large transients in state estimation error, which may be addressed by a linear time-varying KF. The latter is significantly more complex, since the estimator feedback gains must be computed by matrix inversion at every time step. If a nonlinear dynamic model and/or measurement model is available, then an EKF may be implemented. However, the increased amount of computation necessitated at every time step may overwhelm hardware capabilities in the case of most high-speed flows of interest. Moreover, the increasing complexity may even lead to a degradation of fidelity if the filter is not tuned properly.

In this paper, all the preceding estimation strategies were implemented and assessed using a well-established DNS database of a high-speed low-Reynolds-number axisymmetric jet. A time-invariant ROM of the shear layer of this jet using POD and GP has recently been developed. To cover the important region of the end of the potential core, the axial extent of the modeling domain was from 7 to 10 jet diameters downstream of the nozzle exit. The pressure in the irrotational near field has long been surmised to be an ideal measurement for estimating the state of the shear layer in real time. For practical implementation, the pressure sensors should be close to the nozzle exit, upstream of the modeling domain. In the axisymmetric jet, it is meaningful to employ an azimuthal ring array of such sensors in a cross-sectional plane, or a linear array in a meridional plane. In this paper, various permutations and combinations of such arrays were located in the axial domain between 4 and 6 jet diameters downstream of the nozzle exit. An effective configuration was found with a ring array in the middle and two sensors on either side of it forming a uniform linear array over the preceding axial range. Compared with a single ring array, the preceding arrangement improved the estimation accuracy to a greater or lesser extent, depending on the strategy used. The convective time separation between the upstream measurement and the downstream velocity field to be estimated was addressed by making the estimator predictive; this is a significant benefit for feedback control. Another novel approach introduced in this paper is to derive the measurement equation for the dynamic filters using single-time SE.

Single-time LSE was found to be quite unsuitable for the present application, since some states of the model are not linearly related to the pressure signal. QSE yielded significant improvements in accuracy, bearing testimony to the essential nonlinearity in the pressure-velocity coupling. The estimation accuracy of the LTIF was indistinguishable from the linear time-varying KF. The former showed better or equivalent fidelity compared with the quadratic stochastic estimator, thereby demonstrating the distinct benefit to be accrued in moving to a dynamic model-based estimation strategy. It is to be emphasized that the LTIF is similar in complexity to the linear stochastic estimator, and it is considerably less resource intensive than the quadratic stochastic estimator. The EKF is significantly more complicated, but it actually underperformed the linear filters, possibly owing to insufficient tuning.

The DNS database of the unforced jet provides an excellent testbed for determining effective estimation strategies and measurement configurations. The next step would be to implement and validate these ideas in the high-Reynolds-number forced laboratory jet of engineering interest. In spite of the wide disparity in Reynolds numbers, the two jets have been previously found to possess similar

dynamics of the coherent structures of interest. Moreover, there are well-established tools for extending linear estimation models to address forcing. The insight gained through the extensive investigation reported in this paper would be essential in such future endeavors.

Appendix: Implementing Quadratic Stochastic Estimation in a Fourier Domain

Implementing SE consists of three main steps: identifying the product terms to retain among all possible combinations, simplifying the model so that the set of regressors is linearly independent, and determining the set of multiplicative parameters so that the model optimally fits the given data set. For QSE in the Fourier domain, the model proposed in Eq. (13) already addressed the first issue by reference to Remark 4. The second step will be discussed next.

The model proposed in Eq. (13) has different quadratic parameters multiplying product terms that differ only in the order of multiplication. Such terms are not independent; thus, the least-mean-squares problem becomes ill-posed if one tries to determine the associated parameters as distinct entities. A related issue is that all the estimation parameters are known a priori to be real, following arguments made in Remark 2. Thus, for $m = 0$, to avoid redundancies, one formulates the following estimator:

$$\begin{aligned}
\tilde{\alpha}^{(n)}_{\mathrm{QSE},k+N_c\backslash k}(0) &= c_{\mathrm{QSE}}(n,N_c) \\
&+ \sum_{s=1}^{N_p^a} l^a_{\mathrm{QSE}}(s,0,n,N_c)\hat{p}^a_k(x_s,0) + \sum_{s=1}^{N_p^l} l^l_{\mathrm{QSE}}(s,0,n,N_c)p^l_k(x_s) \\
&+ \sum_{m'=0}^{N_m}\sum_{s=1}^{N_p^a}\sum_{s'=1}^{s} Q^{aa}_{\mathrm{QSE}}(s,s',m',-m',n,N_c)\mathcal{R}\{\hat{p}^a_k(x_s,m')\hat{p}^{a*}_k(x_{s'},m')\} \\
&+ \sum_{s=1}^{N_p^l}\sum_{s'=1}^{s} Q^{ll}_{\mathrm{QSE}}(s,s',0,n,N_c)p^l_k(x_s)p^l_k(x_{s'}) \\
&+ \sum_{m'=0}^{N_m}\sum_{s=1}^{N_p^a}\sum_{s'=1}^{N_p^l} Q^{al}_{\mathrm{QSE}}(s,s',m',0,n,N_c)\mathcal{R}\{\hat{p}^a_k(x_s,m')\}p^l_k(x_{s'})
\end{aligned}$$

For $m \neq 0$, the redundancies are removed as follows:

$$\begin{aligned}
\tilde{\alpha}^{(n)}_{\mathrm{QSE},k+N_c\backslash k}(m) &= \sum_{s=1}^{N_p^a} l^a_{\mathrm{QSE}}(s,m,n,N_c)\hat{p}^a_k(x_s,m) \\
&+ \sum_{s=1}^{N_p^l} l^l_{\mathrm{QSE}}(s,m,n,N_c)p^l_k(x_s) \\
&+ \sum_{m'=m-N_m}^{\lfloor m/2\rfloor}\sum_{s=1}^{N_p^a} Q^{aa}_{\mathrm{QSE}}(s,s,m',m-m',n,N_c) \\
&\times \hat{p}^a_k(x_s,m')\hat{p}^a_k(x_s,m-m') \\
&+ \sum_{m'=m-N_m}^{N_m}\sum_{s=2}^{N_p^a}\sum_{s'=1}^{s-1} Q^{aa}_{\mathrm{QSE}}(s,s',m',m-m',n,N_c) \\
&\times \hat{p}^a_k(x_s,m')\hat{p}^a_k(x_{s'},m-m') \\
&+ \sum_{s=1}^{N_p^l}\sum_{s'=1}^{s} Q^{ll}_{\mathrm{QSE}}(s,s',m,n,N_c)p^l_k(x_s)p^l_k(x_{s'}) \\
&+ \sum_{m'=-N_m}^{N_m}\sum_{s=1}^{N_p^a}\sum_{s'=1}^{N_p^l} Q^{al}_{\mathrm{QSE}}(s,s',m',m,n,N_c)\hat{p}^a_k(x_s,m')p^l_k(x_{s'})
\end{aligned}$$

Here, $\lfloor\cdot\rfloor$ denotes the `floor` function.

As in all stochastic estimators, QSE proceeds by defining the mean-square estimation error. It is immediate from the preceding formulations that the QSE model is linear in the estimation parameters, so that the mean-square error surface is a paraboloid in the parameter space. From this stage on, the problem becomes indistinguishable from an LSE, and the solution is well known; see, for example, [65].

The estimation parameters appearing in Eq. (13) can be retrieved from the ones determined previously using the following equations. However, it must be understood that those parameters that appear on the right-hand side of the following equations, but not in the preceding equations, are identically zero:

$$\begin{aligned}
&q^{aa}_{\mathrm{QSE}}(s,s',m',m-m',n,N_c) \\
&\quad = \frac{0.5}{1+\delta_{m,0}}\{Q^{aa}_{\mathrm{QSE}}(s,s',m',m-m',n,N_c) \\
&\qquad\qquad + Q^{aa}_{\mathrm{QSE}}(s',s,m',m-m',n,N_c)\} \\
&\quad + 0.25\{Q^{aa}_{\mathrm{QSE}}(s,s',m-m',m',n,N_c) \\
&\qquad\qquad + Q^{aa}_{\mathrm{QSE}}(s',s,m-m',m',n,N_c)\}, \\
&q^{ll}_{\mathrm{QSE}}(s,s',m,n,N_c) \\
&\quad = 0.5\{Q^{ll}_{\mathrm{QSE}}(s,s',m,n,N_c) + Q^{ll}_{\mathrm{QSE}}(s',s,m,n,N_c)\}, \\
&q^{al}_{\mathrm{QSE}}(s,s',m',0,n,N_c) \\
&\quad = 0.5\{Q^{al}_{\mathrm{QSE}}(s,s',m',0,n,N_c) + Q^{al}_{\mathrm{QSE}}(s,s',-m',0,n,N_c)\}
\end{aligned}$$

Acknowledgments

The research was supported in part by the U.S. Air Force Office of Scientific Research through a joint research program with Syracuse University and Clarkson University, with John Schmisseur as the Program Manager, and by a fellowship from Ohio State University to the first author. The authors would also like to thank J. B. Freund for providing the direct numerical simulation database, Edgar Caraballo for many insightful discussions, and Mark Glauser for the collaboration.

References

[1] Gutmark, E. J., Schadow, K. C., and Yu, K. H., "Mixing Enhancement in Supersonic Free Shear Flows," *Annual Review of Fluid Mechanics*, Vol. 27, No. 1, 1995, pp. 375–417. doi:10.1146/annurev.fl.27.010195.002111

[2] Jordan, P., and Gervais, Y., "Subsonic Jet Aeroacoustics: Associating Experiment, Modelling And Simulation," *Experiments in Fluids*, Vol. 44, No. 1, 2008, pp. 1–21. doi:10.1007/s00348-007-0395-y

[3] Samimy, M., Kim, J.-H., Kastner, J., Adamovich, I., and Utkin, Y., "Active Control of High-Speed and High-Reynolds-Number Jets Using Plasma Actuators," *Journal of Fluid Mechanics*, Vol. 578, 2007, pp. 305–330. doi:10.1017/S0022112007004867

[4] Samimy, M., Kim, J.-H., Kastner, J., Adamovich, I., and Utkin, Y., "Active Control of a Mach 0.9 Jet for Noise Mitigation Using Plasma Actuators," *AIAA Journal*, Vol. 45, No. 4, 2007, pp. 890–901. doi:10.2514/1.27499

[5] Utkin, Y. G., Keshav, S., Kim, J.-H., Kastner, J., Adamovich, I. V., and Samimy, M., "Development and Use of Localized Arc Filament Plasma Actuators for High-Speed Flow Control," *Journal of Physics D: Applied Physics*, Vol. 40, No. 3, 2007, pp. 685–694. doi:10.1088/0022-3727/40/3/S06

[6] Sinha, A., Kim, K., Kim, J.-H., Serrani, A., and Samimy, M., "Extremizing Feedback Control of a High-Speed and High Reynolds Number Jet," *AIAA Journal*, Vol. 48, No. 2, 2010, pp. 387–399. doi:10.2514/1.44012

[7] Sinha, A., Serrani, A., and Samimy, M., "Initial Development of Reduced-Order Models for Feedback Control of Axisymmetric Jets," *International Journal of Flow Control*, Vol. 2, No. 1, 2010, pp. 39–60. doi:10.1260/1756-8250.2.1.39

[8] Freund, J. B., "Noise Sources in a Low-Reynolds-Number Turbulent Jet at Mach 0.9," *Journal of Fluid Mechanics*, Vol. 438, No. 1, 2001, pp. 277–305. doi:10.1017/S0022112001004414

[9] Lumley, J. L., "The Structure of Inhomogeneous Turbulent Flows," *Atmospheric Turbulence and Radio Wave Propagation*, edited by A. M. Yaglom and V. I. Tatarsky, Nauka, Moscow, 1967, pp. 166–178.

[10] Berkooz, G., Holmes, P., and Lumley, J., "The Proper Orthogonal Decomposition in the Analysis Of Turbulent Flows," *Annual Review of Fluid Mechanics*, Vol. 25, No. 1, 1993, pp. 539–575. doi:10.1146/annurev.fl.25.010193.002543

[11] Holmes, P., Lumley, J., and Berkooz, G., *Turbulence, Coherent Structures, Dynamical Systems and Symmetry*, Cambridge Univ. Press, New York, 1996.

[12] Gaitonde, D. V., "Simulation-Based Analysis of the Near Field in a Supersonic Jet Controlled by Plasma Actuators," 49th AIAA Aerospace Sciences Meeting, AIAA Paper 2011-0023, 2011.

[13] Arndt, R. E. A., Long, D. F., and Glauser, M. N., "The Proper Orthogonal Decomposition of Pressure Fluctuations Surrounding a Turbulent Jet," *Journal of Fluid Mechanics*, Vol. 340, No. 1, 1997, pp. 1–33. doi:10.1017/S0022112097005089

[14] Picard, C., and Delville, J., "Pressure Velocity Coupling in a Subsonic Round Jet," *International Journal of Heat and Fluid Flow*, Vol. 21, No. 3, 2000, pp. 359–364. doi:10.1016/S0142-727X(00)00021-7

[15] Coiffet, F., Jordan, P., Delville, J., Gervais, Y., and Ricaud, F., "Coherent Structures in Subsonic Jets: A Quasi-Irrotational Source Mechanism?," *International Journal of Aeroacoustics*, Vol. 5, No. 1, 2006, pp. 67–89. doi:10.1260/147547206775220407

[16] Tinney, C. E., Jordan, P., Hall, A. M., Delville, J., and Glauser, M. N., "A Time-Resolved Estimate of the Turbulence and Sound Source Mechanisms in a Subsonic Jet Flow," *Journal of Turbulence*, Vol. 8, No. 7, 2007, pp. 1–20. doi:10.1080/14685240600928472

[17] Tinney, C. E., Ukeiley, L. S., and Glauser, M. N., "Low-Dimensional Characteristics of a Transonic Jet, Part 2: Estimate and Far-Field Prediction," *Journal of Fluid Mechanics*, Vol. 615, 2008, pp. 53–92. doi:10.1017/S0022112008003601

[18] Kastner, J., Cuppoletti, D., Malla, B., and Gutmark, E., "Simultaneous Measurement of Flow Fluctuations and Near-Field Pressure in a Subsonic Jet," 48th AIAA Aerospace Sciences Meeting, AIAA Paper 2010-1217, 2010.

[19] Adrian, R. J., "On the Role of Conditional Averages in Turbulence Theory," *Turbulence in Liquids: Proceedings of the 4th Biennial Symposium*, Science Press, Princeton, NJ, 1977, pp. 323–332.

[20] Adrian, R. J., and Moin, P., "Stochastic Estimation of Organized Turbulent Structure: Homogeneous Shear Flow," *Journal of Fluid Mechanics*, Vol. 190, 1988, pp. 531–559. doi:10.1017/S0022112088001442

[21] Guezennec, Y. G., "Stochastic Estimation of Coherent Structures in Turbulent Boundary Layers," *Physics of Fluids*, Vol. 1, No. 6, 1989, pp. 1054–1060. doi:10.1063/1.857396

[22] Cole, D. R., Glauser, M. N., and Guezennec, Y. G., "An Application Of The Stochastic Estimation To The Jet Mixing Layer," *Physics of Fluids*, Vol. 4, No. 1, 1992, pp. 192–194. doi:10.1063/1.858486

[23] Adrian, R. J., "Conditional eddies in isotropic turbulence," *Physics of Fluids*, Vol. 22, No. 11, 1979, pp. 2065–2070. doi:10.1063/1.862515

[24] Tung, T. C., and Adrian, R. J., "Higher-Order Estimates of Conditional Eddies in Isotropic Turbulence," *Physics of Fluids*, Vol. 23, No. 7, 1980, pp. 1469–1470. doi:10.1063/1.863130

[25] Naguib, A. M., Wark, C. E., and Juckenhofel, O., "Stochastic Estimation and Flow Sources Associated with Surface Pressure Events in a Turbulent Boundary Layer," *Physics of Fluids*, Vol. 13, No. 9, 2001, pp. 2611–2626. doi:10.1063/1.1389284

[26] Murray, N. E., and Ukeiley, L. S., "Estimation of the Flowfield from Surface Pressure Measurements in an Open Cavity," *AIAA Journal*, Vol. 41, No. 5, 2003, pp. 969–972. doi:10.2514/2.2035

[27] Boree, J., "Extended Proper Orthogonal Decomposition: A Tool to Analyse Correlated Events in Turbulent Flows," *Experiments in Fluids*, Vol. 35, No. 2, 2003, pp. 188–192. doi:10.1007/s00348-003-0656-3

[28] Taylor, J. A., and Glauser, M. N., "Towards Practical Flow Sensing and Control via POD and LSE Based Low-Dimensional Tools," *Journal of Fluids Engineering*, Vol. 126, No. 3, 2004, pp. 337–345. doi:10.1115/1.1760540

[29] Tinney, C. E., Coiffet, F., Delville, J., Hall, A. M., Jordan, P., and Glauser, M. N., "On Spectral Linear Stochastic Estimation," *Experiments in Fluids*, Vol. 41, No. 5, 2006, pp. 763–775. doi:10.1007/s00348-006-0199-5

[30] Caraballo, E., Little, J., Debiasi, M., and Samimy, M., "Development and Implementation of an Experimental-Based Reduced-Order Model for Feedback Control of Subsonic Cavity Flows," *Journal of Fluids Engineering*, Vol. 129, No. 7, 2007, pp. 813–824. doi:10.1115/1.2742724

[31] Pinier, J. T., Ausseur, J. M., Glauser, M. N., and Higuchi, H., "Proportional Closed-Loop Feedback Control of Flow Separation," *AIAA Journal*, Vol. 45, No. 1, 2007, pp. 181–190. doi:10.2514/1.23465

[32] Kastner, J., Harris, C., Mignee, J., and Gutmark, E. J., "Linear Stochastic Estimation of the Flowfield from a Bypass Ratio 8 Nozzle Configuration," 47th AIAA Aerospace Sciences Meeting, AIAA Paper 2009-0072, 2009.

[33] Bonnet, J.-P., Cole, D. R., Delville, J., Glauser, M. N., and Ukeiley, L. S., "Stochastic Estimation and Proper Orthogonal Decomposition: Complementary Techniques for Identifying Structure," *Experiments in Fluids*, Vol. 17, No. 5, 1994, pp. 307–314. doi:10.1007/BF01874409

[34] Ewing, D., and Citriniti, J. H., "Examination of a LSE/POD Complementary Technique Using Single and Multi-Time Information in the Axisymmetric Shear Layer," *Proceedings of the IUTAM Symposium on Simulation and Identification of Organized Structures in Flows*, Lyngby, Denmark, edited by J. Sorensen, E. Hopnger, and N. Aubry, Kluwer Academic, Norwell, MA, 1999, pp. 375–384.

[35] Murray, N. E., and Ukeiley, L. S., "Modified Quadratic Stochastic Estimation of Resonating Subsonic Cavity Flow," *Journal of Turbulence*, Vol. 8, No. 53, 2007, pp. 1–23. doi:10.1080/14685240701656121

[36] Baars, W., Tinney, C. E., and Powers, E. J., "POD Based Spectral Higher-Order Stochastic Estimation," 48th AIAA Aerospace Sciences Meeting, AIAA Paper 2010-1292, 2010.

[37] Durgesh, V., and Naughton, J. W., "Multi-Time-Delay LSE-POD Complementary Approach Applied to Unsteady High-Reynolds-Number Near Wake Flow," *Experiments in Fluids*, Vol. 49, No. 3, 2010, pp. 571–583. doi:10.1007/s00348-010-0821-4

[38] Kalman, R. E., "A New Approach to Linear Filtering and Prediction Problems," *Journal of Basic Engineering*, Vol. 82, No. 1, 1960, pp. 35–45. doi:10.1109/ICASSP.1982.1171734

[39] Jazwinski, A. H., *Stochastic Processes and Filtering Theory*, Academic Press, New York, 1970.

[40] Anderson, B. D. O., and Moore, J. B., *Optimal Filtering*, Dover, New York, 2005.

[41] Bewley, T. R., and Protas, B., "Skin Friction and Pressure: The 'Footprints' of Turbulence," *Physica D*, Vol. 196, Nos. 1–2, 2004, pp. 28–44. doi:10.1016/j.physd.2004.02.008

[42] Pastoor, M., Henning, L., Noack, B. R., King, R., and Tadmor, G., "Feedback Shear Layer Control for Bluff Body Drag Reduction," *Journal of Fluid Mechanics*, Vol. 608, 2008, pp. 161–196. doi:10.1017/S0022112008002073

[43] Ahuja, S., and Rowley, C. R., "Feedback Control of Unstable Steady States of Flow Past a Flat Plate Using Reduced-Order Estimators," *Journal of Fluid Mechanics*, Vol. 645, 2010, pp. 447–478. doi:10.1017/S0022112009992655

[44] Wiederhold, O., King, R., and Noack, B. R., "Robust Control in Turbomachinery Configurations," *Active Flow Control II*, edited by R. King, Springer, Berlin, 2010, pp. 187–201.

[45] Hoepffner, J., Chevalier, M., Bewley, T. R., and Henningson, D. S., "State Estimation in Wall-Bounded Flow Systems, Part 1: Perturbed Laminar Flows," *Journal of Fluid Mechanics*, Vol. 534, 2005, pp. 263–294. doi:10.1017/S0022112005004210

[46] Chevalier, M., Hoepffner, J., Bewley, T. R., and Henningson, D. S., "State Estimation in Wall-Bounded Flow Systems, Part 2: Turbulent Flows," *Journal of Fluid Mechanics*, Vol. 552, 2006, pp. 167–187. doi:10.1017/S0022112005008578

[47] Kastner, J., Samimy, M., Hileman, J., and Freund, J. B., "Comparison of Noise Mechanisms in High and Low Reynolds Number High-Speed Jets," *AIAA Journal*, Vol. 44, No. 10, 2006, pp. 2251–2258. doi:10.2514/1.18384

[48] Rowley, C. R., "Modeling, Simulation, and Control of Cavity Flow Oscillations," Ph.D. Thesis, California Inst. of Technology, Pasadena, CA, 2002.

[49] Sirovich, L., "Turbulence and the Dynamics of Coherent Structures: Parts I–III," *Quarterly of Applied Mathematics*, Vol. 45, No. 3, 1987, pp. 561–590.

[50] Kasnakoğlu, C., Serrani, A., and Efe, M. O., "Control Input Separation by Actuation Mode Expansion for Flow Control Problems," *International Journal of Control*, Vol. 81, No. 9, 2008, pp. 1475–1492. doi:10.1080/00207170701867857

[51] Luchtenburg, D. M., Gunther, B., Noack, B. R., King, R., and Tadmor, G., "A Generalized Mean-Field Model of the Natural and High-Frequency Actuated Flow Around a High-Lift Configuration," *Journal of Fluid Mechanics*, Vol. 623, 2009, pp. 283–316. doi:10.1017/S0022112008004965

[52] Tadmor, G., Lehmann, O., Noack, B. R., and Morzynski, M., "Mean Field Representation of the Natural and Actuated Cylinder Wake," *Physics of Fluids*, Vol. 22, No. 3, 2010, p. 034102. doi:10.1063/1.3298960

[53] Noack, B. R., Papas, P., and Monkewitz, P., "The Need for a Pressure-Term Representation in Empirical Galerkin Models of Incompressible Shear Flows," *Journal of Fluid Mechanics*, Vol. 523, 2005, pp. 339–365. doi:10.1017/S0022112004002149

[54] Franklin, G. F., Powell, J. D., and Workman, M. L., *Digital Control of Dynamic Systems*, Addison–Wesley, Reading, MA, 1990.

[55] Oppenheim, A. V., and Schafer, R. W., *Discrete-Time Signal Processing*, Prentice–Hall, Englewood Cliffs, NJ, 1989.

[56] Ko, N. W. M., and Davies, P. O. A. L., "The Near Field Within the Potential Cone of Subsonic Cold Jets," *Journal of Fluid Mechanics*, Vol. 50, 1971, pp. 49–78. doi:10.1017/S0022112071002453

[57] Zaman, K. B. M. Q., and Hussain, A. K. M. F., "Natural Large-Scale Structures in the Axisymmetric Mixing Layer," *Journal of Fluid Mechanics*, Vol. 138, 1984, pp. 325–351. doi:10.1017/S0022112084000148

[58] Citriniti, J. H., and George, W. K., "Reconstruction of the Global Velocity Field in the Axisymmetric Mixing Layer Utilizing the Proper Orthogonal Decomposition," *Journal of Fluid Mechanics*, Vol. 418, No. , 2000, pp. 137–166. doi:10.1017/S0022112000001087

[59] Jung, D. H., Gamard, S., and George, W. K., "Downstream Evolution of the Most Energetic Modes in a Turbulent Axisymmetric Jet at High Reynolds Number, Part 1: The Near-Field Region," *Journal of Fluid Mechanics*, Vol. 514, No. , 2004, pp. 173–204. doi:10.1017/S0022112004000163

[60] Jordan, P., Tinney, C. E., Delville, J., Coiffet, F., Glauser, M. N., and Hall, A. M., "Low-Dimensional Signatures of the Sound Production Mechanisms in Subsonic Jets: Towards Their Identification and Control," 35th AIAA Fluid Dynamics Conference and Exhibit, AIAA Paper 2005-4647, 2005.

[61] Kearney-Fischer, M., Kim, J.-H., and Samimy, M., "Control of a High Reynolds Number Mach 0.9 Heated Jet Using Plasma Actuators," *Physics of Fluids*, Vol. 21, No. 9, 2009, Paper 095101. doi:10.1063/1.3210771

[62] Ukeiley, L. S., and Ponton, M. K., "On the Near Field Pressure of a Transonic Axisymmetric Jet," *International Journal of Aeroacoustics*, Vol. 3, No. 1, 2004, pp. 43–65. doi:10.1260/147547204323022257

[63] Hall, J., Pinier, J., Hall, A. M., and Glauser, M. N., "Two-Point Correlations of the Near- And Far-Field Pressure in a Transonic Jet," *Proceedings of the Fluids Engineering Summer Meeting*, Miami, FL, American Soc. of Mechanical Engineers FEDSM2006-98458, Fairfield, NJ, 2006.

[64] Tinney, C. E., Glauser, M. N., and Ukeiley, L. S., "Low-Dimensional Characteristics of a Transonic Jet, Part 1: Proper Orthogonal Decomposition," *Journal of Fluid Mechanics*, Vol. 612, 2008, pp. 107–141. doi:10.1017/S0022112008002978

[65] Ljung, L., *System Identification: Theory for the user*, Prentice–Hall, Upper Saddle River, NJ, 1999.

E. Livne
Associate Editor